Interaction dynamics of gap flow with vortex-induced vibration in side-by-side cylinder arrangement

Cite as: Phys. Fluids **28**, 127103 (2016); https://doi.org/10.1063/1.4968587
Submitted: 19 April 2016 • Accepted: 08 November 2016 • Published Online: 08 December 2016

Bin Liu and Rajeev K. Jaiman

PHYSICS OF FLUIDS **28**, 127103 (2016)

Interaction dynamics of gap flow with vortex-induced vibration in side-by-side cylinder arrangement

Bin Liu and Rajeev K. Jaiman[a)]
Department of Mechanical Engineering, National University of Singapore, Singapore 119077, Singapore

(Received 19 April 2016; accepted 8 November 2016; published online 8 December 2016)

A numerical investigation of the vortex-induced vibration (VIV) in a side-by-side circular cylinder arrangement has been performed in a two-dimensional laminar flow environment. One of the cylinders is elastically mounted and only vibrates in the transverse direction, while its counterpart remains stationary in a uniform flow stream. When the gap ratio is sufficiently small, the flip-flopping phenomenon of the gap flow can be an additional time-dependent interference to the flow field. This phenomenon was reported in the experimental work of Bearman and Wadcock ["The interaction between a pair of circular cylinders normal to a stream," J. Fluid Mech. **61**(3), 499–511 (1973)] in a side-by-side circular cylinder arrangement, in which the gap flow deflects toward one of the cylinders and switched its sides intermittently. Albeit one of the two cylinders is free to vibrate, the flip-flop of a gap flow during VIV dynamics can still be observed outside the lock-in region. The exact moments of the flip-flop phenomenon due to spontaneous symmetry breaking are observed in this numerical study. The significant characteristic vortex modes in the near-wake region are extracted via dynamic modal analysis and the interference between the gap flow and VIV is found to be mutual. In a vibrating side-by-side arrangement, the lock-in region with respect to reduced velocity becomes narrower due to the interference from its stationary counterpart. The frequency lock-in occurs and ends earlier than that of an isolated vibrating circular cylinder subjected to an identical flow environment. Similar to a tandem cylinder arrangement, in the post-lock-in region, the maximum vibration amplitudes are escalated compared with those of an isolated circular cylinder configuration. On the other hand, subjected to the influence from VIV, the biased gap flow deflects toward the vibrating cylinder quasi-stably during the frequency lock-in process. This behavior is different from the reported bi-stable regime in a stationary side-by-side arrangement. The analyses show that the flip-flop is associated with a characteristic low flip-flopping frequency, which is dependent upon the values of gap ratio, Reynolds number and the symmetry of the gap flow strength in a time-averaged sense. The disappearance of the flip-flop during the frequency lock-in of vibrating side-by-side arrangements is further investigated through a critical-point concept and a critical vortex merging distance. *Published by AIP Publishing.* [http://dx.doi.org/10.1063/1.4968587]

I. INTRODUCTION

Offshore structures exhibit a great variety of flow-induced vibrations, which pose severe challenges to the design and operation because of the occurrence of large amplitudes and loads. When the structure is free to vibrate in the transverse direction, a strong non-linear coupling between the motion of the structure and the wake vortices exists. A side-by-side canonical arrangement is common in offshore engineering applications, for example, a floating production, storage, and

a)Electronic mail: mperkj@nus.edu.sg

offloading (FPSO) operation, arrays of risers and pipelines, ships travelling in rows within close proximity, and many other side-by-side operations. Chaotic fluctuation and large vibration may occur when two bluff bodies are placed closely. It often causes inevitable damage and potential risk to the offshore structures and may lead to a collision or long-term fatigue failure associated with vortex-induced vibrations and other self-excited instabilities. The phenomenon of vortex-induced vibration (VIV) results in a complex evolution of the shedding frequency which deviates from the Strouhal relation as approaching the natural frequency of the structure, which is referred to as a lock-in of the vortex shedding frequency to the structural frequency. The lock-in range corresponds to a large amplitude oscillatory motion of the bluff body, which is of a practical importance in offshore and marine structures. In most offshore engineering applications, multiple structures are far more common than an isolated structure. The flow patterns and forces are strongly dependent upon the arrangement and the distances between these multiple structures.[2] Furthermore, there is a considerable difference between the fluid-structure coupled response of an isolated cylinder arrangement and multiple cylinder arrangements as a result of the complex effects of vortex-to-vortex, vortex-cylinder, and gap flow interactions. Of particular interest in this work is to understand the dynamics of side-by-side interactions in a uniform flowing stream. We consider the flow around two cylinders in both stationary and vibrating conditions as an idealized model to investigate the effects of side-by-side operations in a practical scenario.

A number of excellent experimental and numerical investigations have been conducted in terms of an isolated circular cylinder[2] and multiple circular cylinders in a tandem,[3–5] side-by-side,[6,7] and staggered arrangement.[8] Among these canonical arrangements in industrial applications, the vortex-induced-vibration (VIV) is one of the important factors causing failures and drawing research interest in improving the design and performance of offshore structures. VIV had been investigated by many authors[9,10] in the past several decades. Its importance to the industry led to numerous scientific researches in the comprehensive reviews.[11–18] However, it is still deemed as a challenge, owing to its complexities pertaining to mechanism, operating environment, and available experimental and numerical analyses. A multi-cylinder system is also common in various civil, mechanical, and nuclear engineering applications. The system poses problems and potential failures when its designed parameters and/or environment factors alter. Understanding the coupling effects between VIV and proximity interference is paramount, and numerous scientific articles were published and reported with regard to the interferences and resultant flow regimes in multi-cylinder systems for basic canonical arrangements.[8,19–22] Particularly flow-induced vibrations in a cross-flow problem caused by the adjacent cylinders are complicated to deal with, especially when the flip-flop is involved in a side-by-side arrangement. During the flip-flop of the gap flow, the gap flow could not maintain its straight path and has a tendency to deflect intermittently with new asymmetric states. This spontaneous broken symmetry is associated with a new kind of fluctuation. This phenomenon was reported in the pioneering works of Bearman and Wadcock,[1] Ishigai *et al.*,[23] Williamson,[24] and Kim.[25] It has been noticed that the wake behind a stationary side-by-side circular cylinder is asymmetric, and the gap flow between the two cylinders is deflected either upward or downward for gap ratio $g^* = g/D \in 0.3 - 1.25$ approximately in a laminar flow, where g is the separation distance between the cylinders and D denotes the diameter of each cylinder.

Within such a small gap ratio, the near-wake region is significantly interfered by the presence of adjacent bluff bodies. Generally speaking, these interference effects in cross-flow problems of cylinders can be classified into two categories, namely proximity interference and wake interference. In the wake interference, the nearby cylinders are downstream and further away from the near-wake region of the upstream one. Those wakes exert periodic perturbations, e.g., vorticity and turbulence, upstream of the nearby cylinders, and influence the flow around the nearby cylinders. This is particularly important for the tandem and staggered arrangements of bluff bodies. While in the proximity interference, e.g., $g^* \lesssim 3$ or 4 in a side-by-side arrangement at the laminar flow,[2] the presence of other bluff bodies affects the vortex formation and vortex-shedding process of the one under investigation.[26] Therefore, the influence on the dynamics of structure is very significant due to the presence of other body. As a result, numerical investigations in the present work are limited between gap ratio $g^* \in 0.3 - 2.5$, particularly $g^* \in 0.3 - 1.25$, in which the proximity-interference and flip-flop phenomena with the symmetry breakdown are paramount. For a bi-stable regime of

the flip-flop, the disparate values of force coefficients, frequencies, and the phase angles on each cylinder can be noticed explicitly. Owing to the unbalanced near-wake regions caused by this asymmetry, the vortex shedding frequency, f_{vs}, is different in each cylinder which is referred to as the two-frequency regime.[27]

Recently, the VIV of a circular cylinder near a stationary wall has been studied by Tham *et al.*,[28] in which the dynamics of the isolated cylinder is subjected to the proximity-interference and the gap flow from the nearby stationary wall. As an analogous case where two cylinders are placed in a side-by-side arrangement, the proximity interference imposes different dynamical characteristic which leads to a change in the trend of the vibration amplitude and frequency domain of the cylinder with respect to the reduced velocity. As reported by Tham *et al.*,[28] the streamwise oscillation was enhanced as compared to that of an isolated cylinder case, as the influence of the boundary layer from the stationary wall. A third response branch was also found within the lock-in region. On the contrary, the flip-flop and frequency-superimposition from the adjacent cylinder in side-by-side arrangements are additional interferences to the near-wake region. The exiting stream of the flow through the cylinder-cylinder gap and cylinder-wall behaves differently, whereby the existing jet of the side-by-side cylinders shows the oscillatory pattern involving a bi-stable regime along the centerline location. It is also noteworthy that the existing experimental studies of the proximity interference are conducted at a higher Reynolds number. In our previous studies,[5,28] it was shown that the essential aspects of the fluid-structure interaction (FSI) and VIV dynamics can be analyzed numerically at lower Re.

Ishigai *et al.*[23] and Kim[25] reported that the biased gap flow between a stationary side-by-side cylinder is bi-stable and switches intermittently through a strong bimodal distribution associated with the spontaneous symmetry breaking. In the present investigation, we consider a special side-by-side circular cylinder arrangement which incorporates an elastically mounted cylinder. Therefore, the coupling between VIV and the gap flow is introduced for the first time. Our study is based on the two questions on the coupled stability exchanges between the VIV dynamics and gap flow interactions. Is there a link between the gap flow with the lock-in frequency resonance? How will the frequency synchronization process affect the gap flow in the vibrating side-by-side cylinder arrangement during the lock-in? It is known that the flip-flop is a highly sensitive bi-stable phenomenon and is directly related to the interaction dynamics of the downstream coherent vortex patterns with the gap flow between the cylinders. Although the cylinder still vibrates within $0.3 \lesssim g^* \lesssim 1.25$, it is believed that the mechanism is different from that of a stationary side-by-side arrangement based on the comparison of the characteristics of the deflected gap flow regime and flip-flop dynamics. To analyze the interaction dynamics and the coupled stability exchanges, we employ recent data analysis techniques namely, Hilbert-Huang Transformation (HHT)[29] and Sparsity-Promoting Dynamic Mode Decomposition (SP-DMD)[30] in frequency and time domains. These techniques are able to decompose the complex data sets and reveal their temporal information of a non-linear dynamic fluid-structure problem, e.g., the instantaneous phase angle and frequency, influential modes, and decay/growing rate of amplitude. They can allow to explore the hidden physical mechanisms of various complex dynamical phenomena. In the present work, HHT is used to analyze the instantaneous phase angle relationships among variables to study the net energy transfer. Through the SP-DMD technique, the dominant DMD modes will be identified to study the stability of the flow field and distinguish the particular DMD modes which are related to the deflected gap flow regime and flip-flop instability associated with the symmetry breaking.

The organization of the article is as follows. The mathematical formulation and the post-processing tools are described in Sec. II. This is followed by the problem description and verification of numerical schemes in Sec. III. In Sec. IV, we next present the characterization of the response dynamics of side-by-side cylinders and discuss the flow physics of the flip-flop phenomenon and VIV in terms of wake topology, response characteristics, force components, phase relations, and frequency characteristics. In the end, we provide the concluding remarks.

II. MATHEMATICAL FORMULATION

A. Governing equation

A numerical scheme implementing Petrov-Galerkin finite-element and semi-discrete time stepping is adopted in the present work to investigate the interaction of incompressible viscous flow with rigid-body dynamics.[31–33] The incompressible Navier-Stokes equations are used in the arbitrary Lagrangian-Eulerian (ALE) reference frame and formulated in the following form:

$$\rho^{\mathrm{f}}\left(\frac{\partial \mathbf{u}^{\mathrm{f}}}{\partial t}\bigg|_{\widehat{x}} + \left(\mathbf{u}^{\mathrm{f}} - \mathbf{w}\right)\cdot\boldsymbol{\nabla}\mathbf{u}^{\mathrm{f}}\right) = \boldsymbol{\nabla}\cdot\boldsymbol{\sigma}^{\mathrm{f}} + \mathbf{b}^{\mathrm{f}} \text{ on } \Omega^{\mathrm{f}}(t), \tag{1}$$

$$\boldsymbol{\nabla}\cdot\mathbf{u}^{\mathrm{f}} = 0 \text{ on } \Omega^{\mathrm{f}}(t), \tag{2}$$

where $\mathbf{u}^{\mathrm{f}} = \mathbf{u}^{\mathrm{f}}(\mathbf{x},t)$ and $\mathbf{w} = \mathbf{w}(\mathbf{x},t)$ are the fluid and mesh velocities, respectively. In Eq. (1), the partial time derivative with respect to the ALE referential coordinate $\widehat{x}$ is constant. Here $\mathbf{b}^{\mathrm{f}}$ represents the body force per unit mass and $\boldsymbol{\sigma}^{\mathrm{f}}$ is the Cauchy stress tensor for a Newtonian fluid which is defined as

$$\boldsymbol{\sigma}^{\mathrm{f}} = -p\mathbf{I} + \mu^{\mathrm{f}}\left(\boldsymbol{\nabla}\mathbf{u}^{\mathrm{f}} + \left(\boldsymbol{\nabla}\mathbf{u}^{\mathrm{f}}\right)^{T}\right), \tag{3}$$

where p, μ^{f}, and $\mathbf{I}$ are the hydrodynamic pressure, the dynamic viscosity of the fluid, and the identity tensor, respectively. A rigid-body structure submerged in the fluid experiences unsteady fluid forces and consequently may undergo flow-induced vibrations if the body is mounted elastically. To simulate the translational motion of a rigid body about its center of mass, the equation along the Cartesian axes is given by

$$\mathbf{m}\cdot\frac{\partial \mathbf{u}^{\mathrm{s}}}{\partial t} + \mathbf{c}\cdot\mathbf{u}^{\mathrm{s}} + \mathbf{k}\cdot\left(\boldsymbol{\varphi}^{\mathrm{s}}(\mathbf{z}_0,t) - \mathbf{z}_0\right) = \mathbf{F}^{\mathrm{s}} + \mathbf{b}^{\mathrm{s}} \quad \text{on} \quad \Omega^{\mathrm{s}}, \tag{4}$$

where $\mathbf{m}$, $\mathbf{c}$, $\mathbf{k}$, $\mathbf{F}^{\mathrm{s}}$, and $\mathbf{b}^{\mathrm{s}}$ are the mass, damping coefficient, and stiffness coefficient vectors for the translational motions, fluid traction, and body forces on the rigid body, respectively. Here Ω^{s} represents the domain occupied by the rigid body and $\mathbf{u}^{\mathrm{s}}(t)$ represents the velocity of the immersed rigid body. The fluid and the structural equations are coupled by the continuity of velocity and traction along the fluid-structure interface.

The new position of the rigid body is updated through a position vector $\boldsymbol{\varphi}^{\mathrm{s}}$, which maps the initial position $\mathbf{z}_0$ of the rigid body to its new position at time t. Let γ be the Lagrangian point on Γ and its corresponding mapping position vector to the new position after the motion of the rigid body is $\varphi(\gamma,t)$ at time t. Since the position and flow field around the moving rigid body is updated continuously, the no-slip and traction continuity conditions should be satisfied on the fluid-body interface Γ,

$$\mathbf{u}^{\mathrm{f}}\left(\boldsymbol{\varphi}^{\mathrm{s}}(\mathbf{z}_0,t),t\right) = \mathbf{u}^{\mathrm{s}}\left(\mathbf{z}_0,t\right), \tag{5}$$

$$\int_{\varphi(\gamma,t)} \boldsymbol{\sigma}^{\mathrm{f}}(\mathbf{x},t)\cdot\mathbf{n}\mathrm{d}\Gamma + \int_{\gamma}\mathbf{F}^{\mathrm{s}}\mathrm{d}\Gamma = 0, \qquad \forall\gamma\in\Gamma, \tag{6}$$

where $\mathbf{n}$ is the outer normal to the fluid-body interface. The characterization of the moving fluid-body interface is constructed by means of the ALE technique. The movement of the internal ALE nodes is constructed by solving a continuum hyperelastic model for the fluid mesh such that the mesh quality does not deteriorate as the displacement of the body increases. For the spatial and material mapping problem, we use classical Neo-Hookean material properties for the ALE variational formulation, which does not entail any additional user-defined remeshing parameter. A partitioned iterative scheme based on a non-linear interface force correction[32] is employed to solve the fluid-rigid body interaction. The coupled fields are updated explicitly, and the interface force correction is formed at the end of each fluid sub-iteration. The scheme relies on a dynamic interface force sequence parameter for stabilizing the coupled fluid-structure dynamics with strong added-mass effects.[32,33] The temporal discretization of both the fluid and the structural equations is formulated in the generalized-α framework, and identical order of interpolation has been used for the primitive variables, which implies their collocated arrangement at discrete nodes.[31] The velocity and pressure

are updated via the restarted Generalized Minimal Residual (GMRES) solver proposed in Ref. 34. The GMRES uses a diagonal preconditioner and a Krylov space of 30 orthonormal vectors. In the current formulation, Newton-Raphson type iterations are implemented to minimize the linearization errors per time step. For the sake of completeness, we next present our post-processing techniques to investigate the flow field features associated with the flip-flop oscillations and to analyze the complex interactions between gap flow and VIV dynamics.

B. Dynamic mode decomposition

To explore the wake flow structures, a dynamic mode decomposition (DMD) procedure is used to capture the essential features of a numerically generated unsteady flow field and to explore various temporal information of the complex dataset as a time sequence of velocity fields.[35] A Singular-Value Decomposition (SVD)-based DMD technique, the so-called Sparsity-promoting Dynamic Mode Decomposition (SP-DMD), is incorporated, which allows us to flexibly identify the dominant modes based on the least-square penalty on the different energy level of each DMD mode.[30] The snapshot-based SP-DMD technique provides an appropriate level of trade-off between the quality of information and the number of modes which is used to approximate the unsteady flow field for feature extraction. In contrast to the standard Fast Fourier Transform (FFT), the SP-DMD analysis is useful to identify the behavior of the different time frequencies occurring during the interaction of the gap flow with the side-by-side wakes. For the sake of completeness, the essential algorithm of SP-DMD is given as follows:

1. Take time-sequential snapshots of the flow field and sort the dataset into two matrices where the columns store values of field variables and the rows contain the data sets collected in each sampling time. Here it is assumed the snapshot data are extracted at constant Δt. The two matrices of snapshots are defined as follows:

$$\Phi_0^{n-1} \coloneqq \left[\theta_0, \quad \theta_1 \quad \dots \quad \theta_{n-1}\right], \tag{7}$$

$$\Phi_1^{n} \coloneqq \left[\theta_1, \quad \theta_2 \quad \dots \quad \theta_{n}\right], \tag{8}$$

   where Φ_1^n is defined as the data set (1) of flow field snapshots until time level n and θ_i is the snapshot data at time level i. It is postulated that the two time snapshots are in a linear relationship and written as

$$\Phi_1^n = A\Phi_0^{n-1}. \tag{9}$$

2. Computing SVD of Φ_0^{n-1} as

$$\Phi_0^{n-1} = U\Sigma V^*, \tag{10}$$

   where U is the m (measurement points) × n (number of time series), Σ is the n × n diagonal matrix, V is the m × n matrix, and n is the rank of the matrix Φ_0.
3. Define the optimal rank-n matrix of A as

$$F_{dmd} = U^*\Phi_1^n V\Sigma^{-1}, \tag{11}$$

   where F_{dmd} determines the optimal low-dimensional representation of the matrix A.
4. Solve for the eigenvectors and eigenvalues of F_{dmd},

$$Y_{dmd}^{-1}F_{dmd}Y_{dmd} = E_{dmd}(\mu_n), \tag{12}$$

   where μ_n is the nth eigenvalue of the DMD mode, and the modes are defined as

$$\kappa = UY_{dmd}. \tag{13}$$

5. The growth/decaying rate and rotational frequency are obtained as

$$\text{Growth/decaying rate} = \text{real}(\log(E_{dmd})), \tag{14}$$

$$\text{rotationary frequency} = \text{imag}(\log(E_{dmd})). \tag{15}$$

6. The optimal amplitude α of each DMD mode, $x_{dmd}(\alpha)$, is obtained by minimizing the least square deviation between the matrix snapshot Φ_0^{n-1} and the linear combination of the DMD modes. This is formulated as

$$\underset{\alpha}{\text{minimize}}\ J(\alpha) := \|\Phi_0^{n-1} - \kappa\ \text{diag}(x_{dmd})V_{and}\|_F^2, \tag{16}$$

where V_{and} is the Vandermonde matrix of E_{dmd}.

7. At this stage, the standard SVD-based DMD algorithm is elaborated and the linear approximation of dataset can be written as

$$\underbrace{\begin{bmatrix}\theta_1, & \theta_2 & \dots & \theta_n\end{bmatrix}}_{\Phi_0^{n-1}} \approx \underbrace{\begin{bmatrix}\kappa_1, & \kappa_2 & \dots & \kappa_n\end{bmatrix}}_{\kappa} \underbrace{\begin{bmatrix}\alpha_1 & 0 & 0\\ 0 & \dots & 0\\ 0 & 0 & \alpha_n\end{bmatrix}}_{diag(x_{dmd})} \underbrace{\begin{bmatrix}1 & \mu_1 & \dots & \mu_1^{n-1}\\ 1 & \mu_2 & \dots & \mu_2^{n-1}\\ \vdots & \vdots & \ddots & \vdots\\ 1 & \mu_n & \dots & \mu_n^{n-1}\end{bmatrix}}_{E_{dmd}:=V_{and}}, \tag{17}$$

where κ is the DMD mode matrix, $dia(x_{dmd})$ is the optimal amplitude of each DMD mode, and E_{dmd} is the eigenvalues of F_{dmd} which describe the temporal behavior (growth/decay rate and frequency) of each DMD mode.

8. The above steps elaborate the standard SVD-based DMD. Next SP-DMD is introduced to select the dominant subset of DMD modes through penalizing the non-zero amplitude DMD modes by

$$\underset{\boldsymbol{\alpha}}{\text{minimize}}\ J(\boldsymbol{\alpha}) + \xi\mathbf{card}(\boldsymbol{\alpha}), \tag{18}$$

where ξ is the manually specified sparsity range and **card** denotes the cardinality function with the L_1-norm of the vector of amplitudes $\boldsymbol{\alpha} := [\alpha_1, \alpha_2, \dots, \alpha_n]^T$. α_i represents the amplitude of its corresponding DMD mode i. For this convex optimization problem in the SP-DMD process, one can flexibly identify the most dominant DMD modes by specifying the sparsity range. Through the properly weighted amplitudes, a superposition of all DMD modes optimally approximates the complete data sequence. The main difficulty lies in the identification of a truncated representation that allows us to capture the dominant and specific components of the flow field by eliminating features that contribute weakly to the physical data sequence. Finally, the DMD allows us to focus on smaller regions where dynamically interesting are expected by the user-specified sparsity structure. With the aid of the Hilbert transformation, the phase angle of the original signal can be computed from the function $M_i(t)$ which provides the information of amplitude and local phase.

C. Hilbert-Huang transformation

Fast Fourier Transform (FFT) can analyze a steady and time-invariant signal. It has been considered as a classical signal analytical technique with its underlying limitations. Flip-flopping causes a random switching of gap flow, in which the frequency and amplitude of fluid dynamics variables are changing over time. A standard FFT may not be able to analyze these signals or data sets in the case of the flip-flop phenomenon. On the other hand, HHT can decompose the unsteady and time-variant signals and reveal their instantaneous information (e.g., instantaneous amplitude and frequency) regardless of the time-variant characteristic of the original signal. HHT consists of two primary analytical techniques. Empirical Mode Decomposition (EMD) decomposes the original signal into different modes (intrinsic mode functions, IMFs) through a recursive subtraction process of IMFs from the original signal, sifting process. This sifting process is controlled by a standard deviation. These resultant IMFs are time-variant (instantaneous frequency and amplitude are not constant with respect to time) signals and each IMF characterizes not only a narrow band with one mode of oscillation but both amplitude and frequency modulations. Following EMD, these intrinsic mode functions undergo Hilbert Transform (HT) which converts a real signal into its corresponding analytical signals. These intrinsic mode functions in EMD are prepared for the HT

analysis to return the accurate information of the signal. The basic steps of HHT are demonstrated as follows:

1. Identify local extrema and link them to form an envelope which are spline fitted.
2. Find the mean values among each pair of local maximum and minimum. These mean values are connected to form a signal and subtracted from the original signal. Repeat this step until the mean-value formed signal satisfies the definition of IMF.
3. Define this signal as IMF_1, subtract it from the original signal, and repeat step 2 to find the rest of the IMFs.
4. Implement the Hilbert transformation on each IMF to explore the temporal information of the original signal. The corresponding analytical signals of each IMF are shown as

$$Z_i(t) = A_i(t) + jB_i(t) = M_i(t)e^{j\Phi_i(t)}, \tag{19}$$

where $M_i(t)$ and $\Phi_i(t)$ are the amplitude and phase angle of each IMF mode, respectively. Here A_i and $B_i(t)$ are the ith IMF and its corresponding Hilbert transform, respectively, and $B_i(t)$ can be expressed as

$$B_i(t) = \frac{1}{\pi} Q \int_{-\infty}^{\infty} \frac{A_i(t)}{t-\tau} d\tau, \tag{20}$$

where Q is the principal value.
5. As a result, the original signal can be decomposed into the summation of IMFs as

$$A(t) = Re(Z^{total}) = Re(\sum_{n=1}^{n} M_i(t)\exp[j \int \omega_i(t)dt]), \tag{21}$$

where $j = \sqrt{-1}$ and $\omega_i(t) = \frac{d}{dt}[\Phi_i(t)]$ is the rotational frequency, and Z^{total} is the summation of all analytical signals of each IMF.
6. Finally the phase angle difference ($\Delta\phi$) between two signals ($s1$ and $s2$) can be achieved through the following equation:

$$\Delta\Phi(t) = \text{imag}(\log(Z_{s1}^{total}(t))) - \text{imag}(\log(Z_{s2}^{total}(t))), \tag{22}$$

After reviewing the numerical formulation and analytical techniques, we next present the problem setup and validation of our coupled fluid-structure solver.

III. PROBLEM DESCRIPTION AND VALIDATION

The schematic diagram of a flow across two identical circular cylinders in a side-by-side arrangement is illustrated in Fig. 1. The top cylinder (*Cylinder*1) is mounted on a spring-damper

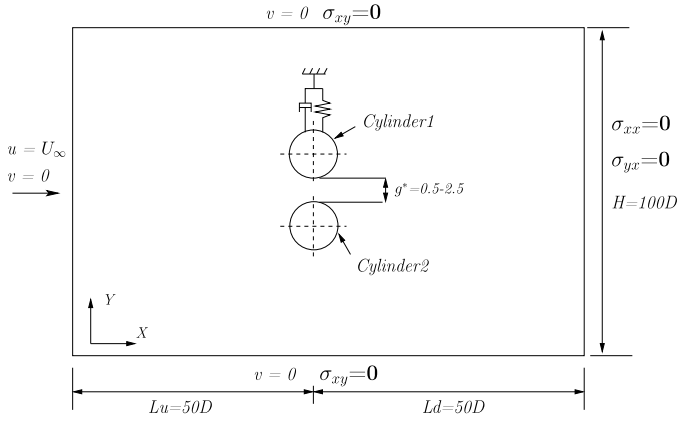

FIG. 1. Schematic diagram of side-by-side cylinders and associated boundary condition details. The top cylinder, *Cylinder*1, is free to vibrate in the transverse direction.

system and is free to vibrate transversely, whereas the bottom cylinder (*Cylinder*2) remains stationary. This special setup will be referred to as a vibrating side-by-side arrangement in Secs. IV and V. The flow direction is parallel to the x-axis from the left toward the right of domain. Here L_u, L_d, and H represent the upstream distance, the downstream distance, and the height of domain, respectively. The upper and lower boundaries of the domain are defined as the slip-wall boundary condition. A uniform free-stream velocity, $U_\infty = 1.0$, is specified on the inlet plane. At the outlet boundary, a traction-free Neumann boundary condition is prescribed.

Apart from the gap ratio $g^* = g/D$, the flow-induced vibration of the side-by-side is characterized by the following parameters:

$$m^* = \frac{4M}{\rho^f \pi D^2} = 10, \tag{23}$$

$$U_r = \frac{U_\infty}{f_n D} \in [2, 10], \tag{24}$$

$$\zeta = \frac{C}{4\pi M f_n} = 0.01, \tag{25}$$

$$Re = \frac{U_\infty D}{\nu} \in [100, 200], \tag{26}$$

where m^*, ρ^f, M, D, f_n, ζ, C, Re, and ν are the mass ratio, the density of fluid, the mass per unit length of cylinder, the diameter of cylinder, the structural natural frequency, the damping ratio, the damping coefficient, the Reynolds number, and the kinematic viscosity, respectively. We consider a representative value of $m^*\zeta = 0.1$, which is typically found in VIV experiments. For physical investigation, the results are post-processed in terms of the following quantities:

$$St = \frac{f_{vs} D}{U_\infty}, \tag{27}$$

$$C_d = \frac{F_x}{\frac{1}{2}\rho^f U_\infty^2 D}, \tag{28}$$

$$C_l = \frac{F_y}{\frac{1}{2}\rho^f U_\infty^2 D}, \tag{29}$$

$$f_{dmd} = \frac{f_w D}{U}, \tag{30}$$

$$A_y^{max} = \sqrt{2} A_y^{rms}, \tag{31}$$

$$x_{cr}^* = \frac{x_{cr}}{D}, \tag{32}$$

$$f_{A_y}^* = \frac{f_{A_y}}{f_n}, \tag{33}$$

where St, f_{vs}, F_x, F_y, C_d, C_l, f_w, f_{dmd}, A_y^{max}, A_y^{rms}, x_{cr}, x_{cr}^*, $f_{A_y}^*$, and f_{A_y} are the Strouhal number, the vortex shedding frequency, the x-component traction force on the cylinder, the y-component traction force on the cylinder, the drag and lift coefficients, the vortex-wake frequency, the normalized vortex modal frequency, the maximum transverse vibration amplitude, the root-mean-squared transverse vibration amplitude, the normalized critical vortex merging distance, the critical distance, the frequency ratio, and the frequency of transverse vibration, respectively. The size of the computational domain is 100D (50D upstream; 50D downstream) × 100D (cross flow direction), which is sufficiently large to reduce the effects of the artificial boundary conditions defined around the fluid domain. A representative computational mesh for the side-by-side cylinders is shown in Fig. 2. The mesh density is finer in the near-wake region from $-2.0D$ to $20.0D$ in the streamwise direction and $6.0D$ to $-6.0D$ in the transverse direction. There is non-deformable structural boundary layer mesh around each cylinder, and the number of nodes on each cylinder is 136 to accurately approximate the dynamics of the unsteady boundary layer. The blockage ratio is fixed at 2% and approximately 50% of the total number of elements is focused around the cylinders and their near-wake regions. Two pairs of diagonal lines are drawn in the domain around cylinders. These

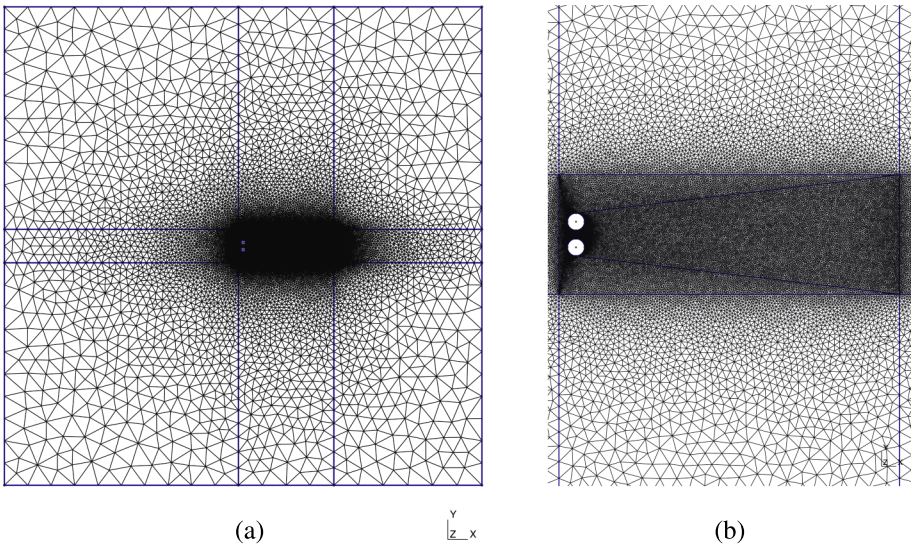

FIG. 2. Representative unstructured mesh distribution for the side-by-side arrangement at gap ratio $g^* = 0.5$: (a) discretization of full domain, (b) the close-up view of mesh around the side-by-side cylinder system.

lines are used to control the exact number of nodes around the essential position in the domain to further refine the particular near-wake region. A mesh convergence study is shown in Table I. The mesh MSH2 is adopted in the present study, as it confirms the adequacy of the numerical results. The average element length in MSH2 around the cylinders is about $0.06D$ and it grows below ratio 1.1 in the near-wake region. All numerical results obtained from the time convergence study (Table II) show a very small deviation among each other. The time step $\Delta t = 0.02$ is adopted in the present study. The percentage of differences in the quantities is listed in the parentheses of tables.

In order to assess the adopted numerical scheme, the results are compared against the available data in the literature. To begin with, the verification of a freely vibrating isolated single cylinder is shown in Fig. 3 with the numerical results[37–39] for both fixed and varying Reynolds numbers. Next, the comparison is performed for the stationary circular cylinders in a side-by-side arrangement at $Re = 100$, $g^* = 1.5$. By seeing from Table III, the hydrodynamic coefficients and Strouhal number have a good agreement with the reported results of Kang[7] and Carini.[36] Besides the aforementioned verifications, a detailed validation of the solver and convergence studies is reported in Refs. 5 and 40 for the freely vibrating isolated cylinder and tandem cylinders. These representative verifications and convergence studies establish the accuracy and validity of the computational method considered in the present investigation for the vibrating side-by-side circular cylinder arrangement.

TABLE I. Mesh convergence study. N_{cyl}: number of points around each cylinder; N_e: total number of elements in the domain; $Re = 100$, $g^* = 1.5$, stationary cylinders in the side-by-side arrangement.

Mesh	MSH1	MSH2	MSH3
Δt	0.02	0.02	0.02
N_{cyl}	68	136	180
N_e	24 854	50 588	101 956
C_d^{mean}	1.434 (0.4%)	1.429 (0.8%)	1.440
C_l^{mean}	0.180 (3.4%)	0.175 (0.6%)	0.174
C_l^{rms}	0.267 (2.6%)	0.260 (0.0%)	0.260
St	0.162 (0.0%)	0.162 (0.0%)	0.162

TABLE II. Time convergence study.

Time Step	C_d^{mean}	C_l^{mean}	C_l^{rms}	St
$\Delta t = 0.08$	1.430 (0.1%)	0.172 (2.3%)	0.2639 (1.1%)	0.165 (1.8%)
$\Delta t = 0.04$	1.429 (0.0%)	0.176 (0.0%)	0.261 (0.0%)	0.162 (0.0%)
$\Delta t = 0.02$	1.429 (0.0%)	0.175 (0.6%)	0.260 (0.4%)	0.162 (0.0%)
$\Delta t = 0.01$	1.429	0.176	0.261	0.162

IV. RESULTS AND DISCUSSION

A. Stationary side-by-side arrangement

Before discussing the coupled interaction between VIV and the gap flow, it is essential to analyze the gap flow interference alone in a stationary side-by-side arrangement. The formation of

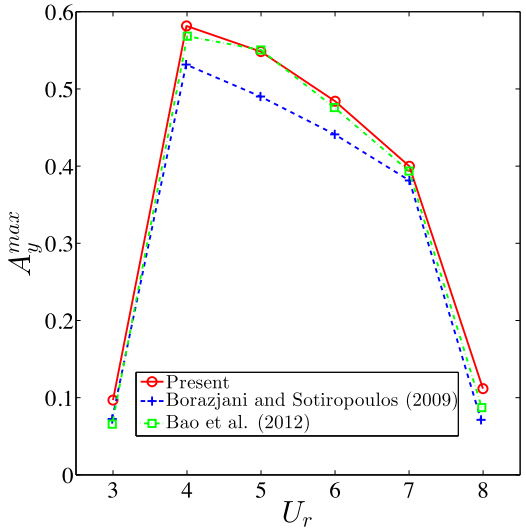

(a)

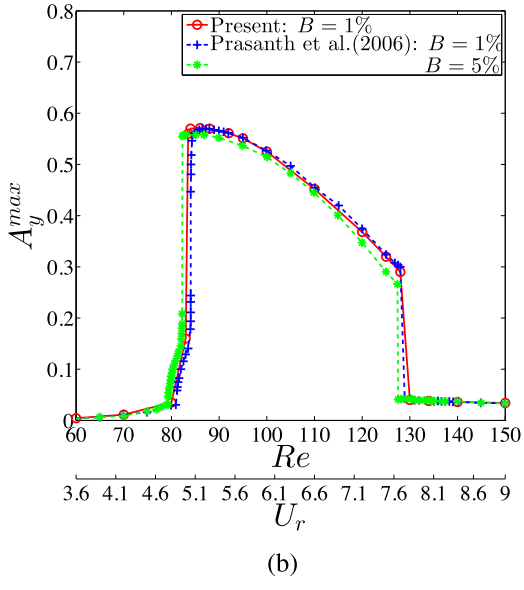

(b)

FIG. 3. Verification of VIV of the freely vibrating isolated circular cylinder for: (a) fixed Reynolds number $Re = 150$, $m^* = 2.55$, and $\zeta = 0$; (b) varying $Re \in 60 - 150$, $m^* = 10$, $\zeta = 0$, and $U_r \in 3.6 - 9$, where B refers to the blockage ratio.

TABLE III. Assessment of hydrodynamic properties for side-by-side cylinders: the mean value of the drag coefficient (C_d^{mean}), the maximum fluctuation of the lift coefficient (C_l^{max}), and the Strouhal number (St).

	C_d^{mean}	C_l^{max}	St
Kang[7]	1.434 (0.3%)	0.271 (0.4%)	0.164 (1.2%)
Carini[36]	1.409 (1.42%)	0.262 (3.8%)	0.163 (0.6%)
Present	1.429	0.272	0.162

the gap flow is discussed at first. Following that, the origins of the deflected gap flow regime and flip-flop phenomenon are reviewed and elaborated with numerical results. Finally, the modes of the vortex formation which are responsible to the deflected gap flow regime and other phenomena are dynamically extracted. Their mechanisms and characteristics are elaborated through the frequency analysis and vortex formation in the side-by-side wakes.

The gap flow comprises two shed counter-rotating shear layers from the inner sides of the cylinders and is a function of gap ratio g^*. In a typical cross flow problem of stationary side-by-side arrangements, a range of flow regimes appear at different g^*. In a laminar flow ($Re \lesssim 198$), the flow regime around these two cylinders behaves like a single bluff body with a base-bleeding for $g^* \lesssim 0.3$. The gap between the cylinders is so narrow that the vortex shedding on the inner sides of the cylinders is significantly suppressed. A single von Kármán vortex street is formed downstream of both cylinders. On the other hand, $g^* \gtrsim 0.3$ is wide enough to allow the shear layers shedding from the inner side of cylinders. They attach to each other and form a gap flow. However, after $g^* \gtrsim 1.25$, the influence of the gap flow tends to reduce. As sketched in Fig. 4(a), since the vortices in both shear layers rotate in the opposite direction, both velocities on the interface of these two shear layers points in the positive x-axis direction. As a result, the jet fluid between these two shear layers is accelerated, and the local pressure is significantly lower than the reference pressure. As shown in Fig. 4(b), these two shear layers attach to each other and manifest itself as a gap flow which possesses its own characteristic dynamic in the near-wake region. Beyond $g^* \approx 2.7$, the interaction between the shear layers of the inner side of cylinders is further weakened. There is only a weak coupling between the wakes. Most of the time, the vortex shedding is in anti-phase with occasional in-phase vortex wake patterns. More details on the wake development and flow regime will be discussed in Sec. IV D.

The deflected gap flow regime imposes a significant interference to the hydrodynamic coefficients. Fig. 5 shows the mutual responses of C_l from both cylinders, and there are net lift forces repelling each other in the opposite directions. Analogous to the near-wall cylinder arrangements,[28] it attributes to the displacement of two stagnation points on the cylinder. Additionally a beating phenomenon is observed in C_l from Figs. 5(a) and 5(b). In the present analysis, observing from Fig. 5, this beating phenomenon is only observed in the flip-flop regime, $g^* \in 0.3 - 1.25$ of a stationary side-by-side arrangement. Therefore, it is evident that it should be associated with the gap flow instabilities. It is known that the cylinder with a narrower near-wake region has higher f_{vs} and its counterpart has a relatively lower f_{vs}. They mutually represent a forcing source to each other in their proximity exerting a local disturbance to the vortex-shedding processes on both cylinders. While the two vortex-wakes with extremely similar frequencies simultaneously occur in a close vicinity, a beating phenomenon can be observed in our study. However, owing to the gap flow dynamics and instabilities (e.g., flip-flop), f_{vs} on each cylinder varies instantaneously as the gap flow. As a result of this strong nonlinear coupling of downstream wakes, its beating behavior cannot be explained simply as a linear superimposition. As g^* increases, the values of C_l on both cylinders approach to the values corresponding to the isolated stationary cylinder.

The analytical description of the flow regime becomes subtle when a jet fluid is ejected into the near-wake of two cylinders. In the flip-flop regime, the gap flow does not follow its original straight path in the streamwise direction. Instead, it deflects to either side of a side-by-side arrangement. The corresponding cylinder with the deflected gap flow has a narrower near-wake region than its counterpart. Furthermore, this deflected gap flow switches between two stable states at a relatively

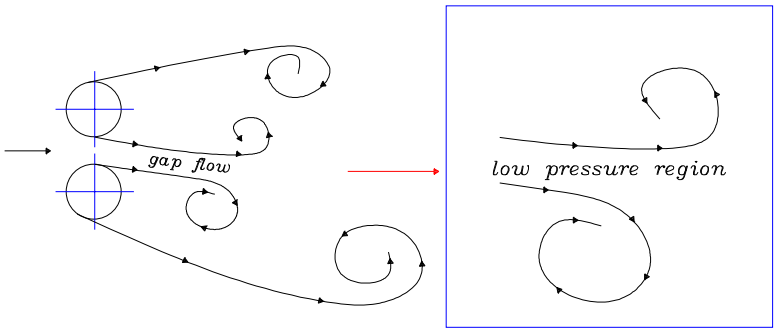

(a)

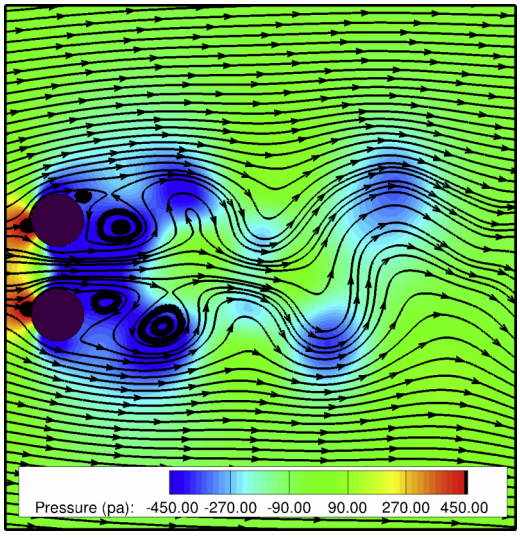

(b)

FIG. 4. Gap flow between two side-by-side circular cylinders: (a) illustration of the gap flow and low pressure region, (b) pressure contour of the gap flow region in a side-by-side arrangement at $Re = 100$ and $g^* = 0.8$.

low frequency which is few orders of magnitude lower than the vortex shedding frequency. This is generally referred to as a flip-flop of the gap flow. There are some debates regarding the origins and mechanisms of the deflected gap flow regime and the flip-flop. Ishigai *et al.*[23] proposed that the deflected gap flow is caused by the Coanda effect. It implies that the gap flow should attach to its adjacent solid bodies and follow their curvatures. However, the flip-flop was also observed on a pair of side-by-side flat plates.[1,24] Besides flat plates, a biased gap flow was also observed in a cross flow problem of an isolated circular cylinder which has a slot across its diameter section.[41] This implies that the deflected gap flow regime is insensitive to the overall geometry of its adjacent bluff bodies, and the Coanda effect is not the root cause of the deflected gap flow regime and flip-flop.

Alam *et al.*[42] also conjectured that the completely symmetric structure in a side-by-side arrangement is a critical condition in which it rises ambiguity to the gap flow choosing its preferred direction. This implies that providing an artificial slight asymmetry in the structure, the gap flow should prefer to a particular direction against the other. However, it is intuitively arguable that the vortex pair and gap flow in the wake should be completely symmetric (anti-phase) in a perfectly symmetric side-by-side arrangement. How come the flow regime is asymmetric and unstable? Furthermore, of the present investigation of vibrating side-by-side arrangements in Sec. IV B, the flip-flop is also observed in pre- and post-lock-in. Hence, the deflected gap flow regime and flip-flop are not explicitly dependent on the perfect symmetric topography. Bearing with these puzzling

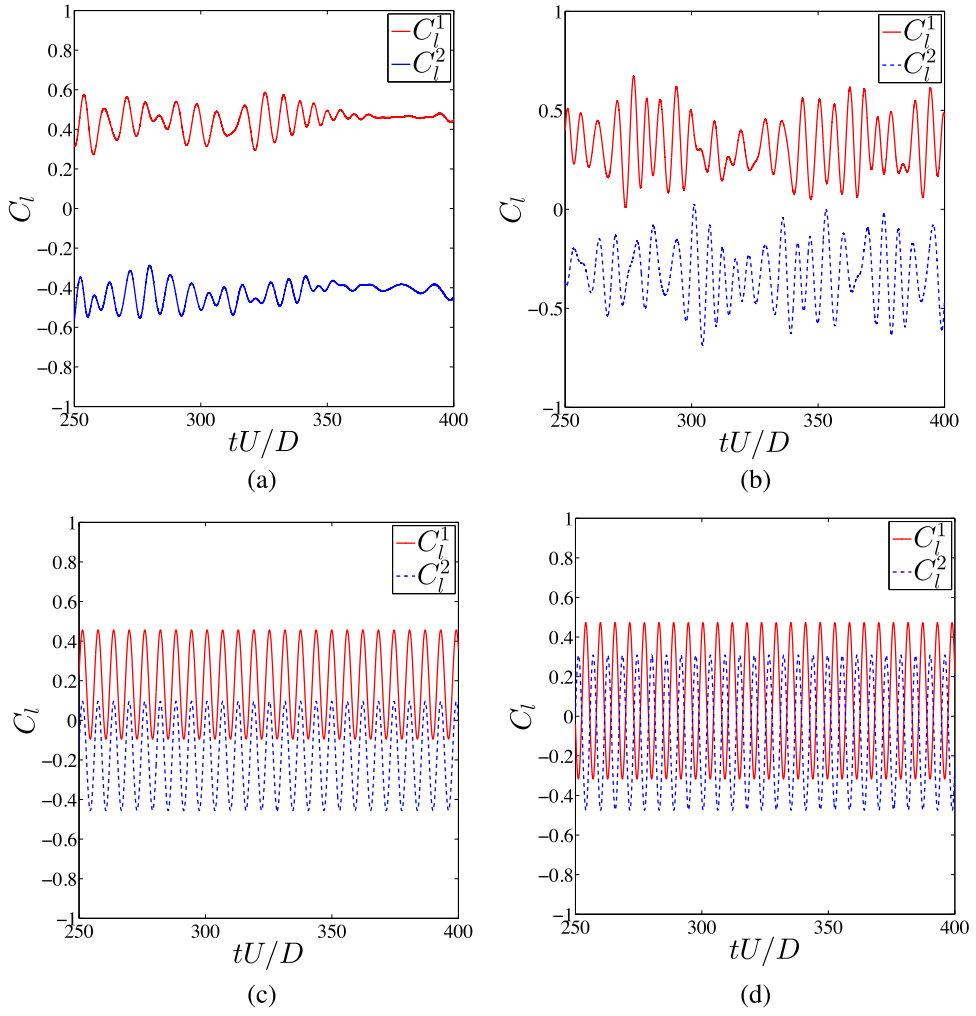

FIG. 5. Time history of the C_l variation of stationary cylinders in a side-by-side arrangement for the gap flow mode: $g^* =$ (a) 0.5, (b) 0.8; and the coupled vortex mode: $g^* =$ (c) 1.5, (d) 3.0.

questions, some authors have attempted to think this ambiguity in a different manner. It is well known that a Hopf bifurcation triggers a von Kármán vortex street, an in-phase vortex synchronization, behind an isolated circular cylinder exceeding a critical Reynolds number ($Re \approx 48$). Analogously, it was reported[43] that a deflected gap flow regime is also associated with a type of bifurcation, namely the pitchfork bifurcation, in the near-wake region of a stationary side-by-side cylinders. Similar to an isolated cylinder case, a Hopf bifurcation causes an in-phase vortex synchronization farther downstream at $Re \gtrsim 60$. Based on the analysis of these two bifurcations, Mizushima and Ino[43] stated that the deflected gap flow and the in-phase vortex synchronization are sensitive to the Reynolds number and the region of the in-phase vortex synchronization will approach to the near-wake region gradually as Re increases further.

All the aforementioned findings show that the deflected gap flow regime in side-by-side cylinders is an intrinsic characteristic of fluid flow. The fluid will inherently deflect toward one side when Re exceeds a particular critical value in a side-by-side arrangement at a specific g^*. This result was also shown by modeling the dynamics of the deflected gap flow regime through a system of two coupled Landau oscillators.[44] It was illustrated that the (stable) deflected gap flow regime and the flip-flop were formed for different reasons. However, the root causes of the flip-flop and its relationship to the deflected gap flow regime were still not revealed at that moment. Inspired by the predecessors' work, Carini *et al.*[36] reported that the flip-flop of the gap flow was a result of

the coupling between the in-phase vortex synchronization (Hopf bifurcation) and the deflected gap flow regime (pitchfork bifurcation). It was deemed as a secondary instability in the near-wake flow field. Subjected to the additional fluctuation associated with the in-phase vortex synchronization, the flow overcomes the barrier between these two stable modes and switch-over occasionally as the secondary instability associated with new spontaneous symmetry breaking. The development of flip-flop as a secondary instability is clearly illustrated in Fig. 6, as the in-phase synchronization

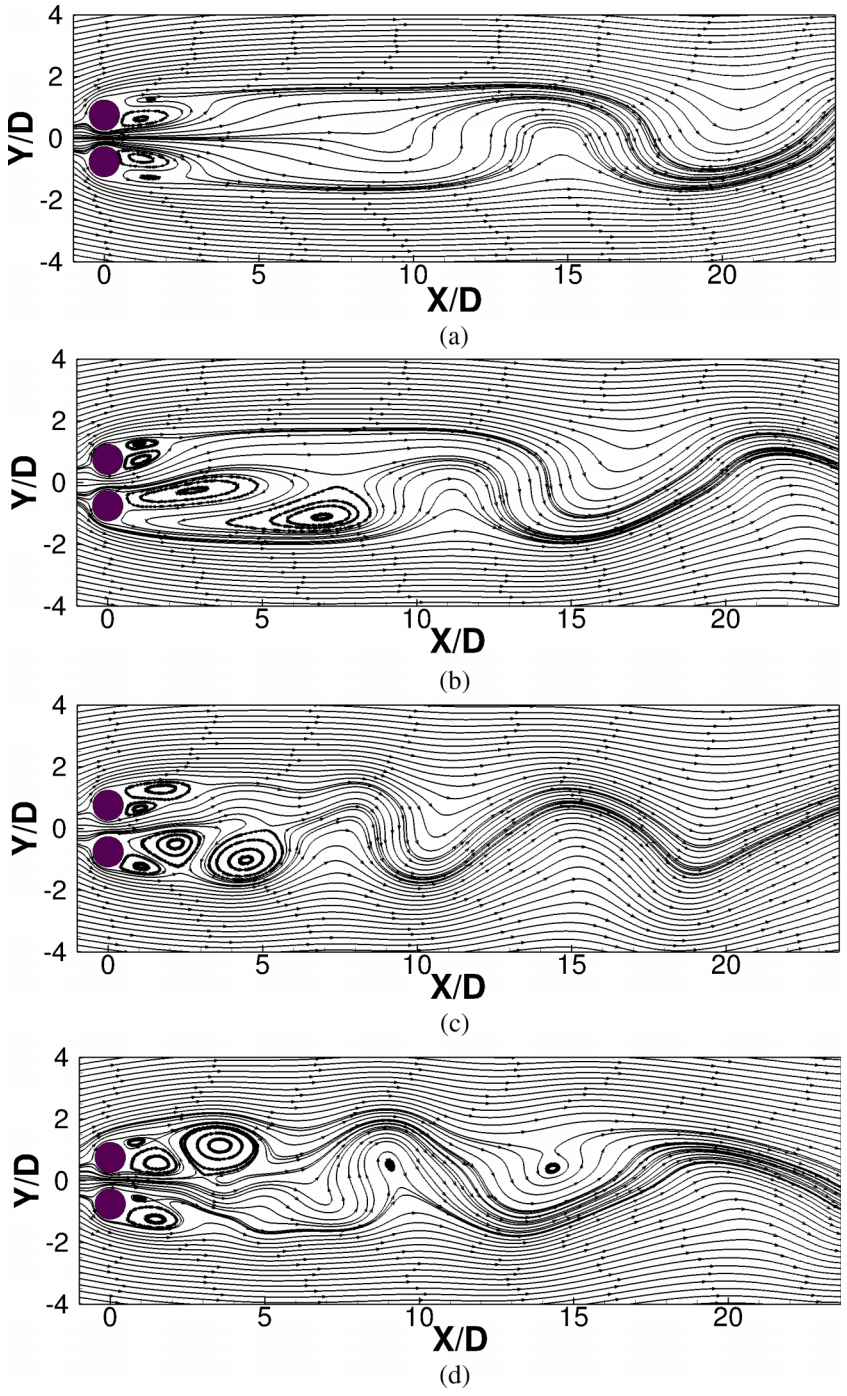

FIG. 6. Streamline plots of stationary cylinders in a side-by-side arrangement at $g^* = 0.5$ and $Re \in 60 - 92$. (a) $Re = 60$, (b) $Re = 70$, (c) $Re = 90$, (d) $Re = 92$.

region approaching the near-wake region where it couples with the pitchfork bifurcation associated with the primary deflected gap flow. Based on the present numerical results for side-by-side circular cylinders, the deflected gap flow regime occurs at $Re \approx 70$ and the flip-flop occurs at $Re \approx 92$ at $g^* = 0.5$.

To analyze the flip-flop phenomenon in detail, it is essential to exactly observe its evolution and underlying mechanism. The flip-flop was usually reported by many authors as an intermittent switch-over of the gap flow (i.e., sudden phase variation from 0° to 180°) due to the complex nonlinear coupling of the two bifurcation modes. However, when exactly this happens was not previously recorded in a time history manner. Here the HHT analysis is able to extract the instantaneous temporal behavior of the hydrodynamic variables, as shown in Fig. 7, to observe the flip-flop frequency exactly. For the ease of observation, the phase angle difference ($\Delta\phi$) is defined in the first and second quadrants. Consistent with the previous reportings, it is observed that the switch-over moment of the gap flow is associated with an instantaneous in-phase vortex shedding synchronization. Based on that, the flip-flop instants are observed in Fig. 7(d) as instantaneous zero phase angle difference ($\Delta\phi = 0°$), in-phase. However, $\Delta\phi = 0$ condition of drag force C_d does not convey the same information of the flip-flop. The lift is directly associated with the vortex shedding process, but the drag is related to the pressure and shear stress in the streamwise direction. This is observed before the vortex shedding occurs at $Re \approx 48$, in which the drag can be observed instead of the lift. In a

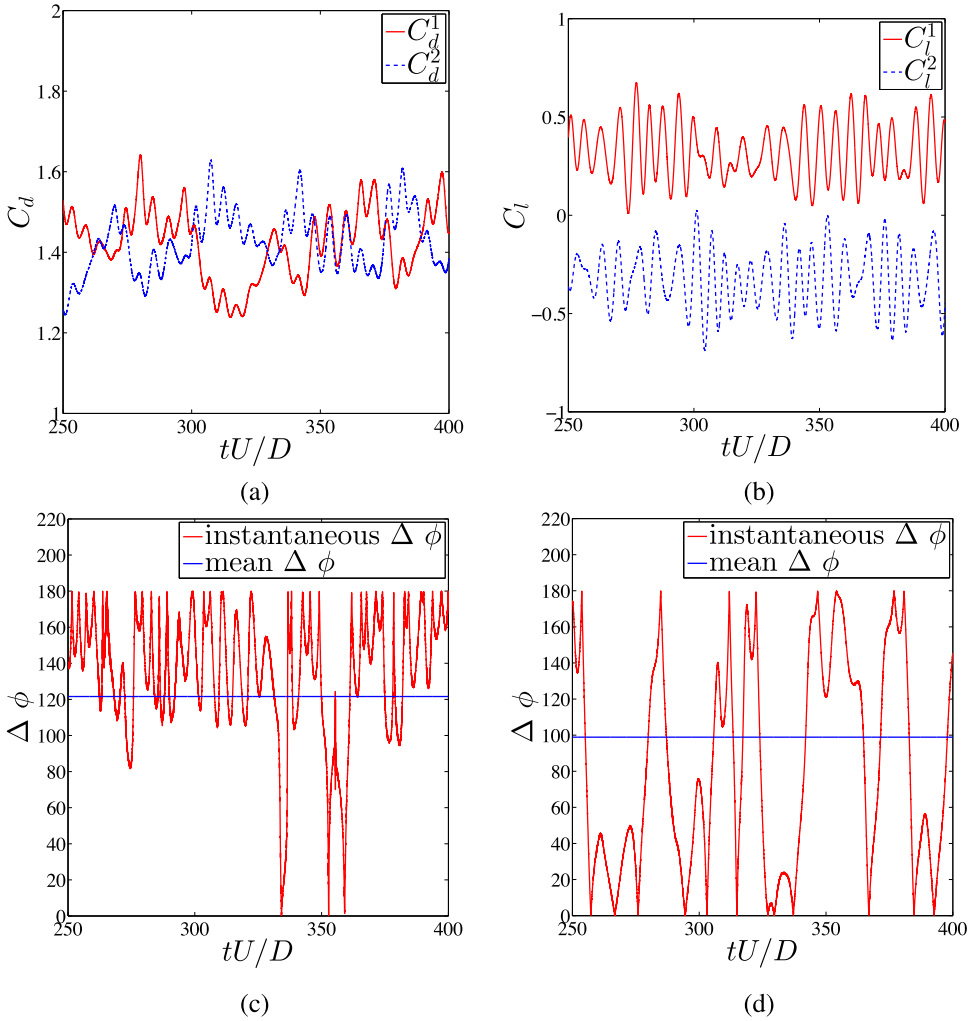

FIG. 7. Time history of the instantaneous phase angle difference between ((a),(c)) C_d, ((b),(d)) C_l of stationary cylinders in a side-by-side arrangement at $Re = 100$ and $g^* = 0.8$. Here ϕ represents the phase angle.

classical cross-flow problem on a stationary circular cylinder in a laminar flow, the frequency of C_d is twice of its corresponding C_l. However, in a stationary side-by-side arrangement, due to the presence of the proximity interference by its counterpart, the wake interference of the gap flow (e.g., deflected gap flow regime) and the gap flow instability (e.g., flip-flop), the C_l behavior cannot be easily and directly interpreted from the evolution of its C_d. Therefore, the temporal behavior of C_l is chosen to interpret the flip-flop phenomenon of the gap flow, instead of C_d. It can be seen that the occurrence frequency of $\Delta\phi = 0^\circ$ is not a constant. Therefore, it confirms the observations in the previous experimental and numerical investigations. In fact, it is a turbulence-like characteristic that poses challenges from a physics viewpoint even at low Reynolds number. It is natural to ponder such questions, for example, what influences the flip-flop frequency? What is the correlation between the flip-flop phenomenon and the corresponding gap flow? Through the present numerical observations, it is realized that the flip-flop dynamics is significantly influenced by the gap flow strength. Although these details will be discussed in Sec. IV D, one should realize that since its randomness associated with a strongly coupled non-linear nature, the classic analytic approaches are not sufficient to extract its characteristics. Therefore, the SP-DMD analysis is adopted in Secs. IV A and IV B to deal with its time-dependent multi-frequency and multi-amplitude characters.

Next, the DMD analysis is performed in stationary side-by-side arrangements at $g^* = 0.5$ between $60 < Re < 100$ to trace the evolution of various DMD modes of the vortex wakes and the identification of relevant flow structures. The frequency spectra are sketched in Figs. 8(a) and 8(b) with the red crosses which represent the relatively influential DMD vortex modes whose dominant eigenfunctions generate a set of dynamically relevant modal structures. They are selected based on the penalization of non-zero values of α with a pre-set sparsity level. The SP-DMD technique allows us to extract a concentration of low-frequency modes, thereby eliminating information with substantially larger amplitudes identified by the standard DMD procedure. To interpret the significance of each relevant frequency, their corresponding DMD modes are plotted in Fig. 8 from (c) to (j). The extraction of influential DMD modes is based on the value of modal amplitude α, the distinct vortex pattern, and significance to the research objective. For a cluster of DMD modes at similar f_{dmd}, they normally share a resembling vortex pattern representing analogous significance to a particular phenomenon. Therefore a representative DMD mode is extracted among them to illustrate a particular problem. Although a particular cluster of DMD modes possesses a high α value, the significance it conveys might be out of the relevancy of the flow structure. As a result, one can see that the DMD mode in Fig. 8(c) has zero frequency and represent the mean flow across the stationary side-by-side cylinders. Figs. 8(d) and 8(g) depict a similar vortex pattern originated from the entry of the gap flow at $Re = 70$ and $Re = 95$, respectively. Interestingly, it is not observed at $Re = 50$ of the same arrangement before the occurrence of the pitchfork bifurcation. Since the deflected gap flow regime is Reynolds-number dependent, it implies that this particular DMD mode should manifest the characteristic of the pitchfork bifurcation, the breakdown of the gap flow symmetry, and triggering of the deflected gap flow regime. The DMD modes in Figs. 8(e) and 8(f) represent the DMD modes of farther-downstream Hopf bifurcation which influence C_l and C_d, respectively. This is assessed based on the characteristic vortex wake pattern in each mode. For example, the DMD mode in Fig. 8(e) possesses a counter-signed vortex wake pair in the streamwise direction. Knowing that this vortex pattern is constant in the DMD mode and the wake strength varies with its corresponding frequency f_{dmd}, it could generate a periodically varying pressure difference in the transverse direction and results in a fluctuation of lift force. Similarly Fig. 8(f) shows a counter-signed vortex wake pattern in the transverse direction, analogous to a counter-rotating side-by-side cylinder arrangement. As the periodical variation of its vortex wake strength, it renders a pressure force fluctuation in the streamwise direction and accounts for the streamwise drag/thrust. Based on analogous reasoning, the modes in Figs. 8(i) and 8(j) at $Re = 95$ affect its corresponding C_l and C_d as well. Logically, after explaining the DMD modes which influence C_d, C_l, and pitchfork bifurcation, it is believed that the mode in Fig. 8(h) is related to the flip-flop phenomenon. This deduction is based on the following four observations. At first, it only presents a vortex pattern in the near-wake region, $0.1D \lesssim X/D \lesssim 5D$, similar to Fig. 8(g). Second, similar to Fig. 8(g), the vortex mode in Fig. 8(h) mainly manifests in $1.5D \lesssim Y/D \lesssim -1.5D$. Its origin of vortex is stretching from the origin point $(0.0D, 0.0D)$, which means that it is related

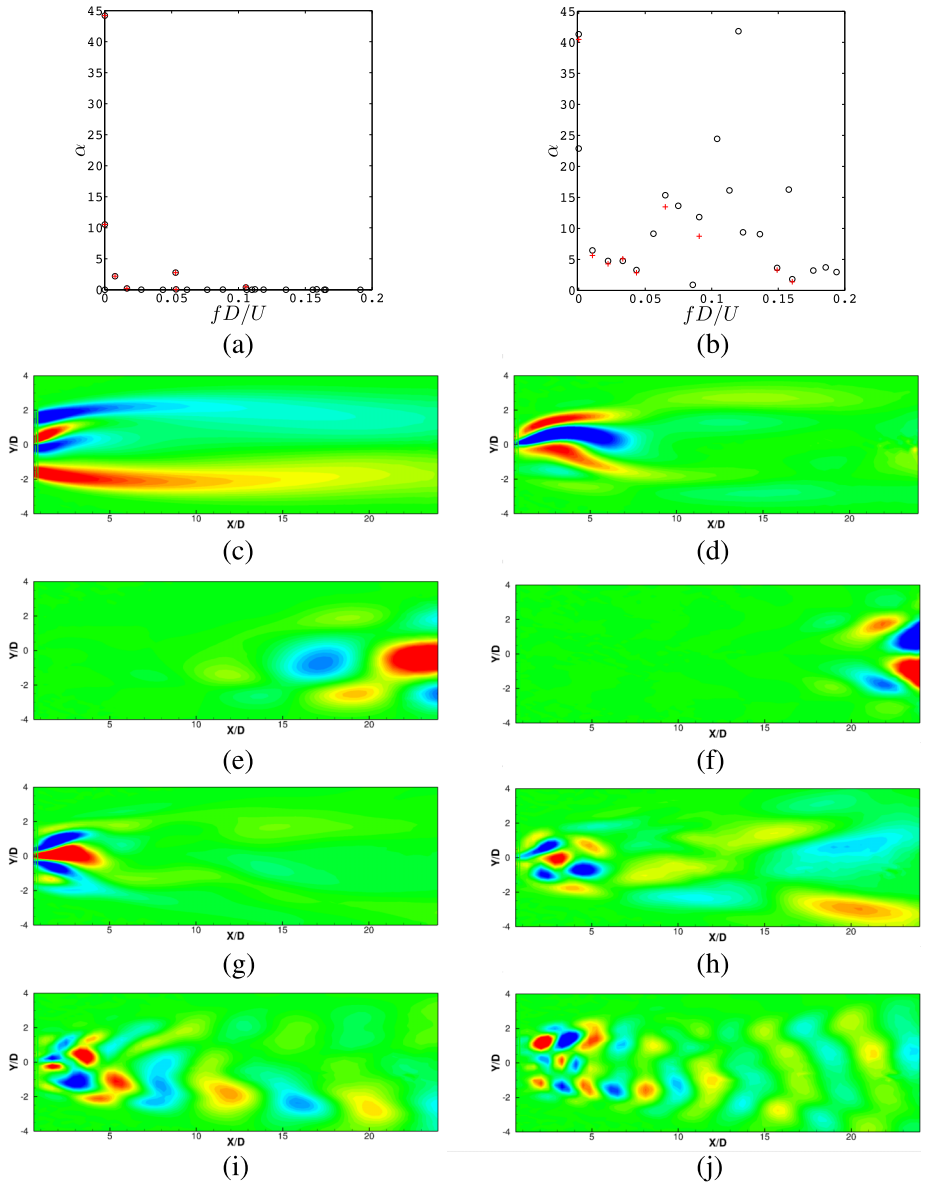

FIG. 8. Dynamic modal analysis for stationary cylinders in a side-by-side arrangement at $g^* = 0.5$: dependence of DMD amplitudes on frequency for (a) $Re = 70$, (b) $Re = 95$, the four representative DMD modes for different frequencies (c)-(f) $Re = 70$; (g)-(j) $Re = 95$. Here circles denote the standard DMD data and crosses represent its sparsity-promoting variant.

to the gap flow behavior. On the other hand, different from Fig. 8(g), it seems disconnected and shows no footprint from the origin point $(0.0D, 0.0D)$, but a secondary instability associated with the symmetry breaking developed from the vortex interactions in the near-wake region. Third, its f_{dmd} is an ideal match with the characteristic $f_{flip} \approx 0.035$ of this case. Furthermore, it does not only exist in this particular case, but the rest of the cases of a stationary side-by-side arrangement in the flip-flop regime. Fourth, the vortex mode in Fig. 8(h) at $f_{dmd} \approx 0.035$ only appears and becomes strong in the near-wake region during the flip-flop regime, where the pitchfork and Hopf bifurcations superimpose. Therefore, it is believed that it indeed represents a primary characteristic mode of the flip-flop. Our conjecture is again confirmed through the DMD analysis in the same arrangement at $Re = 100$. The results in Fig. 9(a) extract the dominant DMD modal frequencies and its corresponding DMD modes, which are plotted in Fig. 9 from (c) to (f). The frequencies of DMD modes mainly center about the four clusters at 0.02, 0.035, 0.085, and 0.17 approximately,

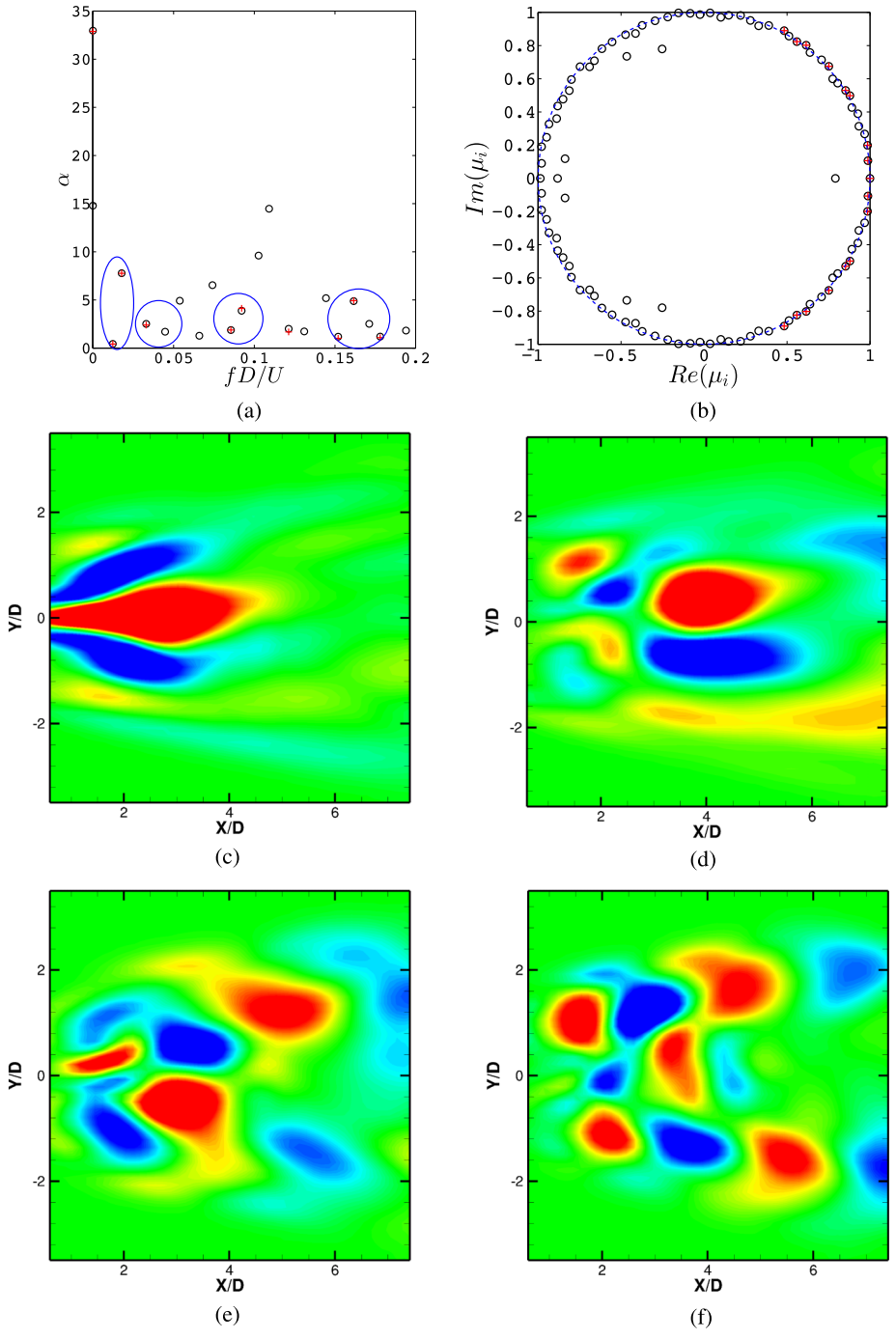

FIG. 9. Dynamic modal analysis for stationary cylinders in a side-by-side arrangement at $Re = 100$ and $g^* = 0.5$: dependence of DMD amplitudes on (a) frequency, (b) eigenvalue spectrum, and flip-flop spatial instability is observed via DMD modes for different frequencies and amplitudes in (c)-(f). The dashed curve identifies the unit circle. The results are obtained using the standard DMD algorithm (circles) and the sparsity-promoting DMD (crosses). (a) $f_{dmd} = fD/U$ vs. α, (b) $Re(\mu_n)$ vs. $Im(\mu_n)$, (c) $f_{dmd} = 0.018$ and $\alpha = 7.6$, (d) $f_{dmd} = 0.034$ and $\alpha = 2.5$, (e) $f_{dmd} = 0.087$ and $\alpha = 4.2$, (f) $f_{dmd} = 0.162$ and $\alpha = 6.1$.

which are marked with blue circles. Based on the aforementioned observations, the modes in Fig. 9 from (c) to (f) should represent DMD modes of the deflected gap flow regime, the flip-flop, C_l, and C_d, respectively. In Fig. 9(b), it also shows that all the DMD modes are stable in the time domain, whereby the unstable mode should be outside the unit circle.

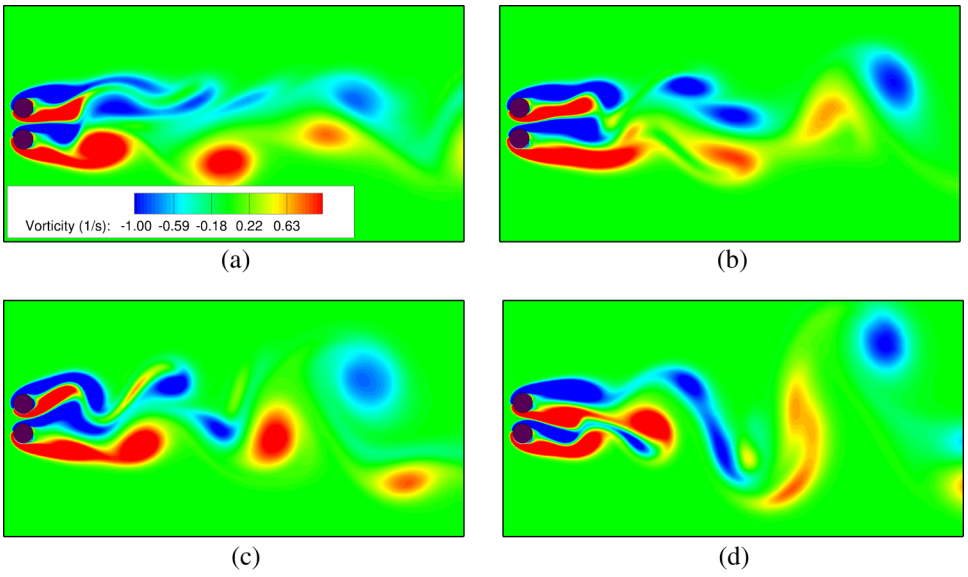

FIG. 10. Vorticity contour plots of a transversely vibrating cylinder in a side-by-side arrangement at $Re = 100$, $m^* = 10$, $\zeta = 0.01$, and $g^* = 0.6$: U_r = (a) 2, (b) 4, (c) 6, (d) 8. The flow is from left to right.

B. Vibrating side-by-side arrangement

If one of the side-by-side cylinders is free to vibrate, the entire flow regime is completely different during the lock-in. To the best of our knowledge, this interaction of gap flow and VIV is not reported in the literature for this arrangement. In this section, the primary focus is on the demonstration of the observations in a vibrating side-by-side arrangement. Similar to the stationary side-by-side cylinder arrangement, g^* refers to the beginning distance between the two cylinders. In terms of the detailed mechanism of VIV and the gap flow interaction, it will be furnished in Secs. IV C and IV D.

As discussed in Sec. IV A, the flow regime of a stationary side-by-side cylinder is already very complex. In a vibrating side-by-side arrangement, it is observed that the biased gap flow deflects toward the side of a vibrating cylinder quasi-stably during lock-in. The sampling vortex contour plots at different U_r values are shown in Fig. 10. In a frequency lock-in, f_{vs} is synchronized with f_n and the transverse vibration motion becomes the active forcing source to control f_{vs}. Therefore, A_y should be chosen as an indicator of the vortex-shedding process, instead of C_l. However, one of the cylinders is stationary in the present vibrating side-by-side arrangement. Therefore, C_l is still valid to be used to investigate the flip-flop behavior for the vibrating side-by-side arrangements during the lock-in and they are plotted in Fig. 11. Observing from Fig. 11, the phase difference $\Delta\phi$ between drag C_d and lift C_l of the two cylinders is approximately 0° and 90°, respectively. Therefore, the flip-flopping behavior ($\Delta\phi = 0$ of C_l) never manifests. Similar to the DMD analysis in a stationary side-by-side cylinder, the modal analysis is performed for the vibrating side-by-side cylinders to reveal the discrepancy between the corresponding stationary and vibrating side-by-side arrangements. It is found that the characteristic DMD mode of the pitchfork bifurcation is not extracted during lock-in, as shown in Fig. 12. On the other hand, the DMD modes at $f_{dmd} = 0.12$ and 0.23 only manifest significantly from $X/D \gtrsim 15$ and responsible for the in-phase synchronization farther downstream, and Figs. 12(b) and 12(d) account for the VIV of the vibrating cylinder. Nonetheless, it is still discernible in the non-lock-in region as shown in Fig. 13. To our understanding, there is a potential characteristic of VIV during lock-in which may account for this change and the frequency synchronization. During the frequency lock-in, f_{vs} of the vibrating cylinder is synchronized with f_n such that Strouhal relation does not fulfill. Moreover, during lock-in the locked vibration is deemed as a forced periodic disturbance which synchronizes the vortex shedding process of the stationary cylinder. As a result, the large single vortex street, as shown in Figs. 12(a) and 12(c), is formed farther downstream because of the in-phase vortex synchronization. Although the frequencies are

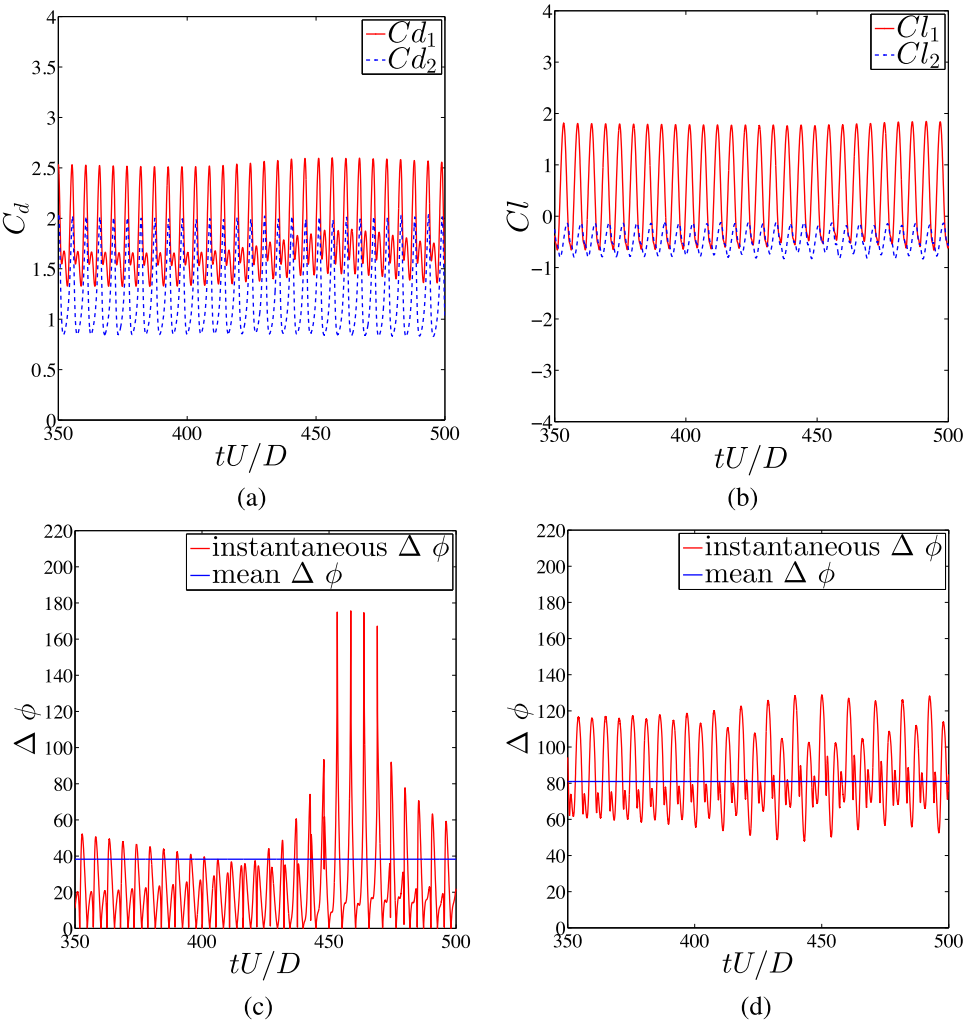

FIG. 11. Time history of the instantaneous phase angle difference between ((a),(c)) the drag force C_d and ((b),(d)) lift force C_l of the transversely vibrating cylinder in a side-by-side arrangement at $Re = 100$, $g^* = 0.6$, and $U_r = 5$.

synchronized, as previously shown in Fig. 11(d), the lift force C_l from cylinders are 90° out of phase. It means that there is no net energy transfer among cylinders and the transverse vibration is fully developed. On the contrary, the drag C_d is generally in-phase ($\Delta\phi \approx 0°$). If the cylinder is allowed to vibrate in the x-direction, the in-phase fluctuation of C_d may intensify the streamwise vibration significantly.

C. The gap flow and VIV interaction

During the frequency lock-in, the response of hydrodynamic forces with respect to U_r is significantly affected. For instance, as depicted in Sec. IV A, a beating effect is observed in stationary side-by-side arrangements at $g^* \lesssim 0.8$. A similar beating effect can also be observed in the vibrating side-by-side arrangement during pre- and post-lock-in. Although the gap flow deflects during lock-in, f_{vs} on both cylinders is still synchronized. Therefore, no beating effect is observed in the frequency lock-in of vibrating side-by-side cylinders. Besides the beating effect, in Fig. 14(a) as U_r falls outside lock-in, the vibration of the cylinder is not much significant and C_d^{mean} on two cylinders is almost identical. This is also the case for the corresponding stationary side-by-side arrangement. On the contrary, the vibrating cylinder always has a relatively high C_d^{mean} during lock-in. This could be induced by the deflected gap flow regime which was documented in

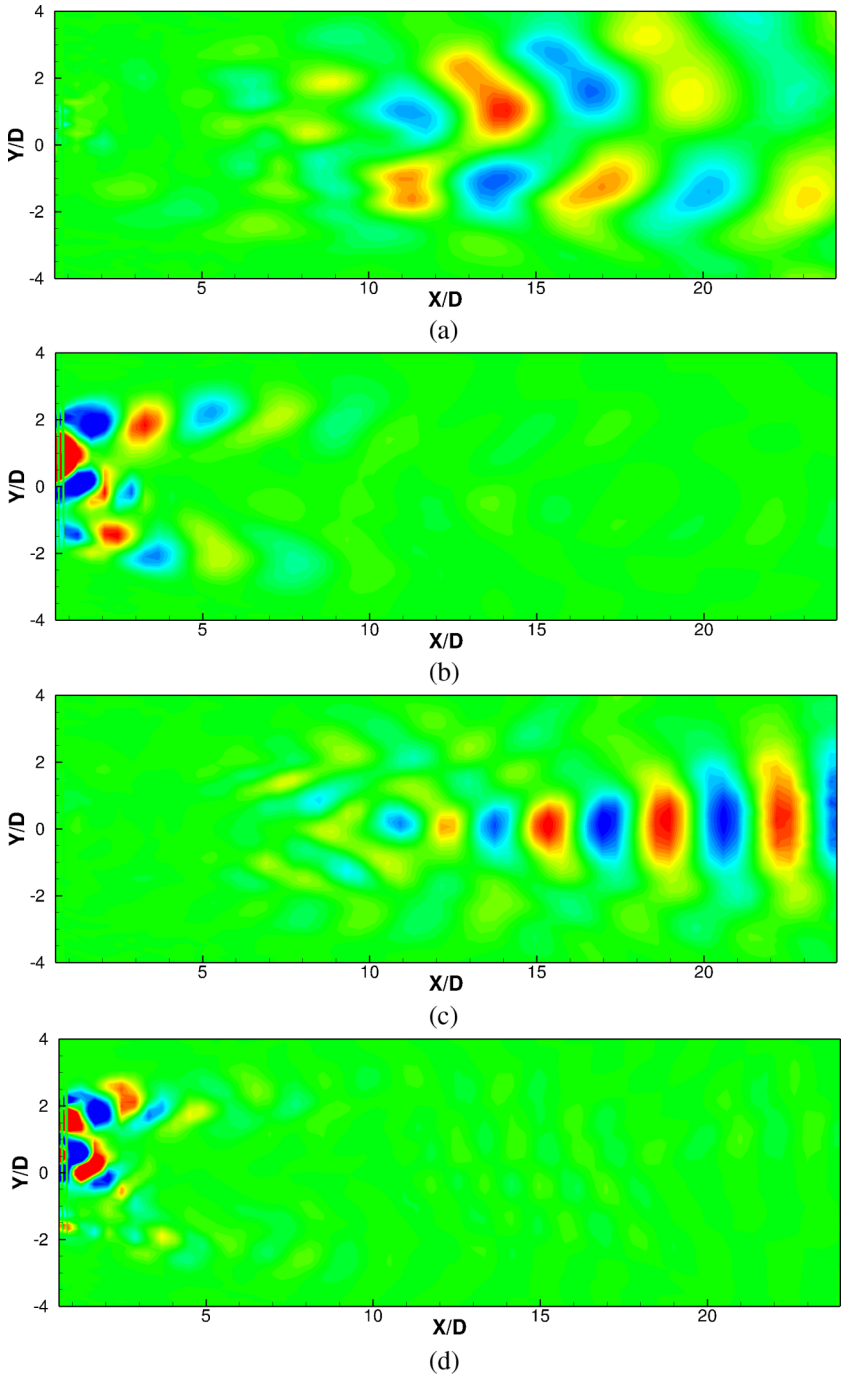

FIG. 12. Dynamic modal analysis for flow in the coupled wake of cylinders in a side-by-side arrangement at $Re = 100$, $m^* = 10$, $\zeta = 0.01$, $g^* = 0.5$, and $U_r = 5$, where *Cylinder*1 vibrates in the transverse direction. (a) $f_{dmd} = 0.12$ and $\alpha = 0.8$, (b) $f_{dmd} = 0.19$ and $\alpha = 17.8$, (c) $f_{dmd} = 0.23$ and $\alpha = 2.8$, (d) $f_{dmd} = 0.38$ and $\alpha = 7.1$.

literatures.[1,7] In the pre- and post-lock-in regimes, owing to the benign vibration compared with the response during lock-in, the overall hydrodynamic responses are resembling the stationary side-by-side arrangement. Therefore, as shown in Fig. 14(b), C_l^{rms} from both cylinders is almost identical. Furthermore, there is also a tendency of C_l^{rms} build-up as g^* decreases. This variation in lift C_l is probably caused by the stagnation point displacement on each cylinder, as a result of the downstream wake interaction.[5] In pre- and post-lock-in regions, as g^* diminishing the displacement

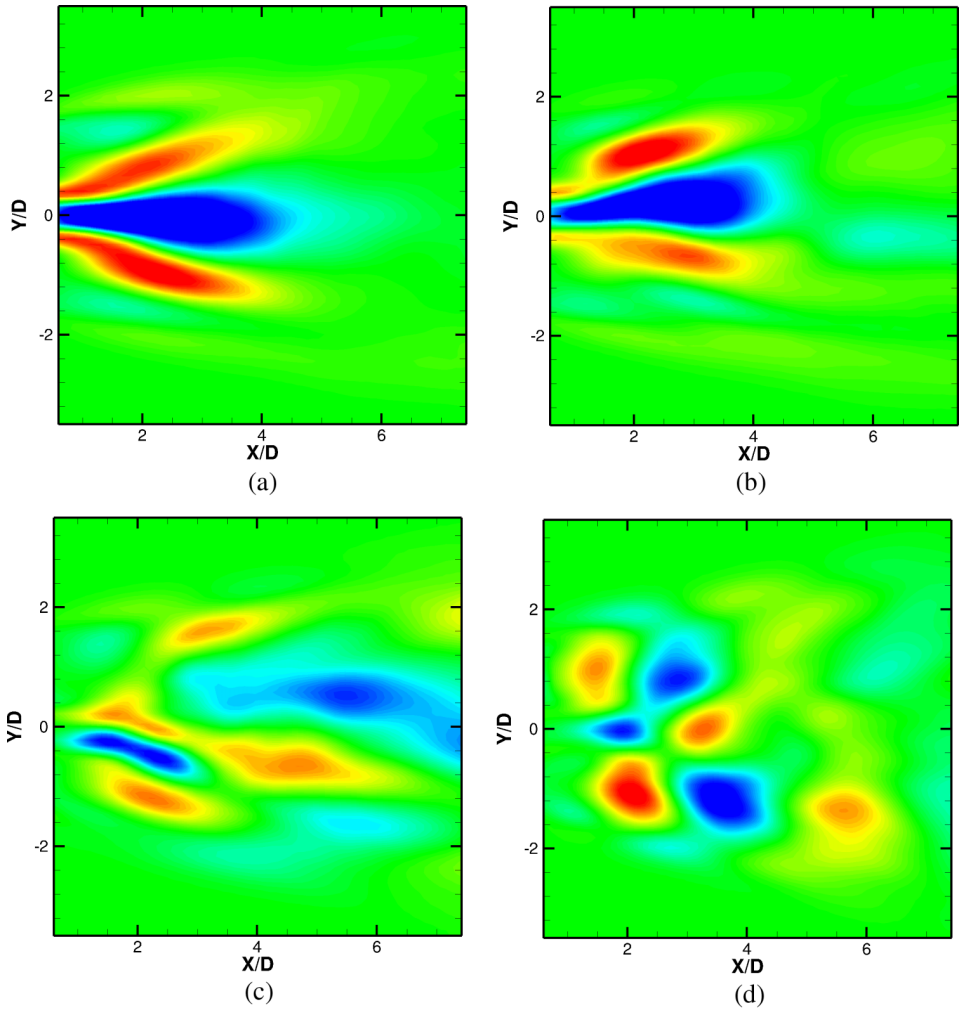

FIG. 13. Dynamic modal analysis for flow in the wake of cylinders in a side-by-side arrangement at $Re = 100$, $m^* = 10$, $\zeta = 0.01$, $g^* = 0.6$ and $U_r = 2$, where *Cylinder*1 vibrates in transverse direction. (a) $f_{dmd} = 0.012$ and $\alpha = 12.2$ (b) $f_{dmd} = 0.03$ and $\alpha = 10.4$ (c) $f_{dmd} = 0.064$ and $\alpha = 4.7$ (d) $f_{dmd} = 0.14$ and $\alpha = 9.2$.

of stagnation points move further into the gap between the side-by-side arrangement. Consequently, C_l^{rms} on each cylinder is higher and results in a distinction of C_l^{rms} among different g^*. On the other hand, C_l^{rms} on the vibrating cylinder is further amplified during lock-in. This is probably induced by the relative motion between the wake flow and cylinder, besides the further displacement of the stagnation point caused by the vibration. The transverse force C_l^{rms} on the stationary cylinder is also increased because of the synchronization from its vibrating counterpart. This proximity interference exerted by its vibrating counterpart during its lock-in is gradually weakening, while g^* exceeding beyond the flip-flop regime, as shown in Fig. 14(b). The gap flow interference to the VIV dynamics can be conspicuously observed through the investigation of A_y^{max} of the vibrating cylinder. As shown in Fig. 14(c), the lock-in region becomes narrower (approximately 43%) and occurs earlier (approximately 11%) than the isolated oscillating cylinder under an identical flow environment. A_y^{max} at different g^* has a mean value which is close to that of the corresponding isolated oscillating cylinder setup. Particularly, at $g^* = 2.5$ where two cylinders are relatively far away from each other, the lock-in region is inclined to restore the characteristic trajectory of the corresponding isolated cylinder case. However, its value exhibits a significant fluctuation (approximately 9%) about its mean value at different gap ratios g^*.

All these discrepancies are associated with the mutual interaction between the gap flow and VIV dynamics. As the gap flow bends toward the vibrating cylinder, the near-wake region of the

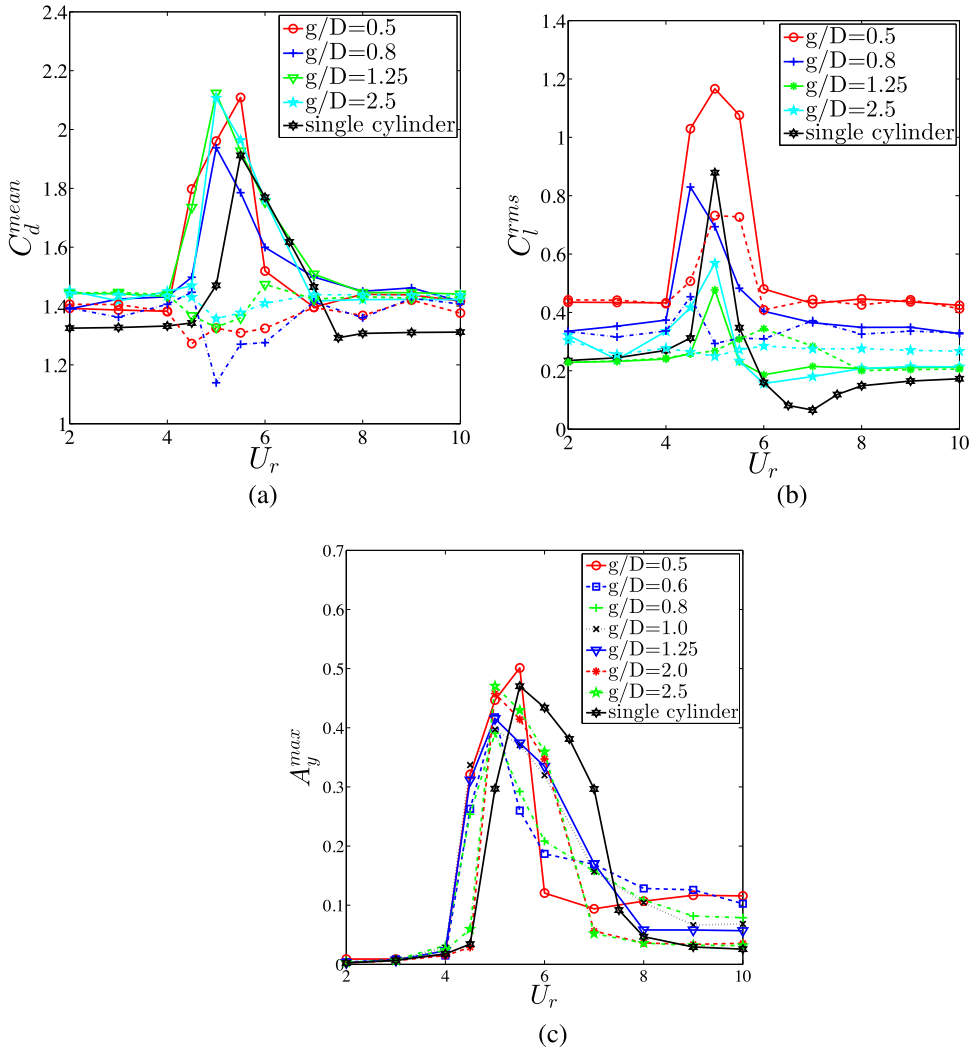

FIG. 14. Dependence of (a) mean drag C_d^{mean}, (b) fluctuating transverse force C_l^{rms}, and (c) A_y^{max} on U_r of a side-by-side arrangement at $Re = 100$, $m^* = 10$, and $\zeta = 0.01$, where *Cylinder*1 vibrates in the transverse direction.

vibrating cylinder becomes narrower and enhances the interaction of the shed shear layers. Therefore f_{vs}, shown in Fig. 15(a), becomes larger than an isolated oscillating cylinder under the identical Re and U_r. Consequently, the cylinder in the current arrangement experiences an enhanced f_{vs} and synchronizes earlier with f_n of the cylinder. Similarly, the mismatch of frequency, the end of the lock-in region, is expected to happen earlier as well. However, albeit the gap flow deflects to the vibrating cylinder during lock-in, as shown in Fig. 15(b), f_{vs} on each cylinder is synchronized to f_n precisely. To elaborate this modulation of the lock-in region in detail, the dependency of the vibration frequency ratio ($f^*_{A_y} = f_{A_y}/f_n$) on U_r, where f_{A_y} refers to the transverse vibrating frequency, is plotted in Fig. 15(c). It should be taken note that f_{A_y} is intermittently changing over time in the deflected gap flow regime. Therefore, $f^*_{A_y}$ is measured in a time-averaged manner except the frequency-discontinuity at the instants of flip-flop. By comparing Figs. 14(c) and 15(c), the onset of VIV indeed occurs earlier ($U_r \approx 4.5$) than the isolated vibrating cylinder at $Re = 100$. Obviously the lock-in region for $g^* = 2.0$ is drastically reduced by about 43% compared with an isolated cylinder at $Re = 100$. Its onset does not occur early. This is probably due to a relatively large g^* at its initial stage. However by the end of the lock-in region, as the extensive transverse vibration, the proximity interference exerted by its stationary counterpart becomes relatively strong (but not enough to suppress the supply of the vortex wake, similar to the $g^* \lesssim 0.3$ cases in the

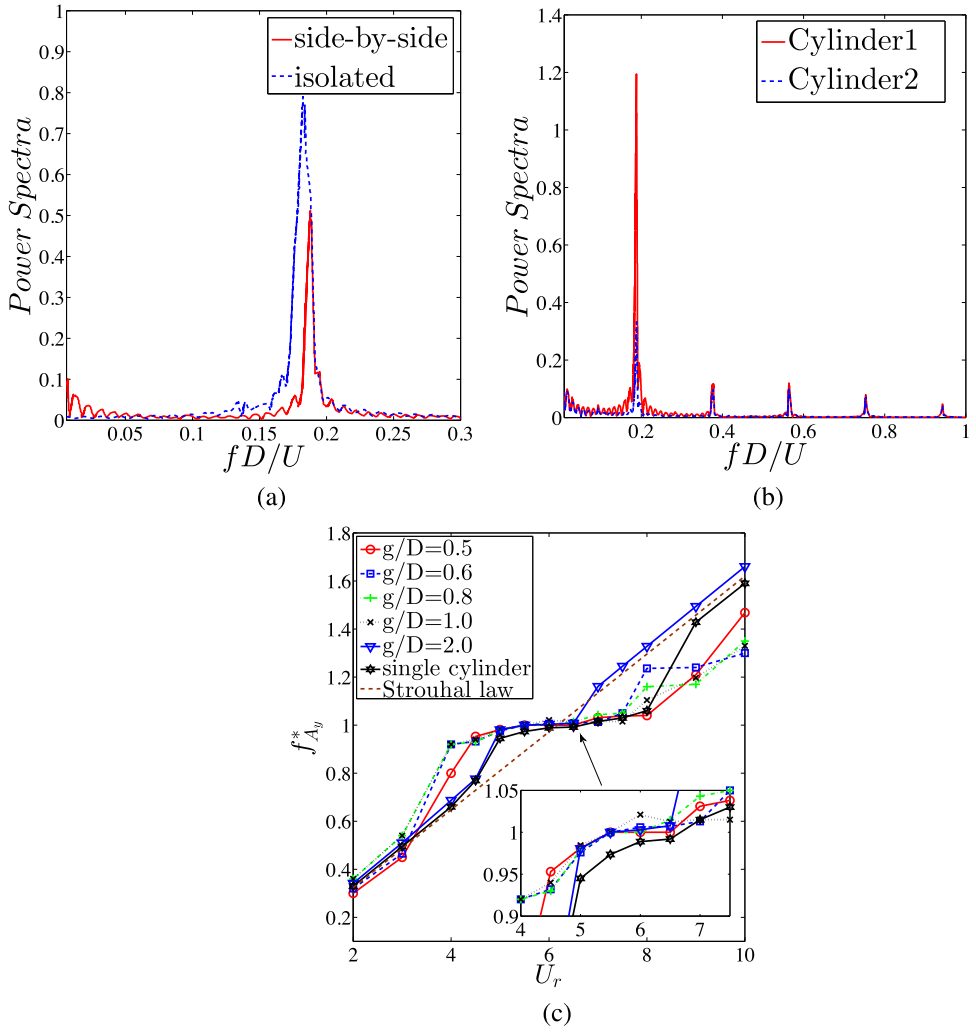

FIG. 15. Spectral analysis at $Re = 100$, $m^* = 10$, and $\zeta = 0.01$: (a) comparison of C_l frequency at $U_r = 5$ for the isolated vibrating cylinder and the vibrating cylinder in a side-by-side arrangement at $g^* = 0.5$; (b) comparison of C_l frequency for cylinders in a side-by-side arrangement at $g^* = 0.5$ and $U_r = 5$, where *Cylinder*1 vibrates in the transverse direction; (c) dependence of the normalized response frequency $f^*_{A_y} = f_{A_y}/f_n$ on the reduced velocity U_r of cylinder in a side-by-side arrangement for varying $g^* \in 0.5-2.0$, where *Cylinder*1 vibrates in the transverse direction.

laminar flow) and induces the frequency mismatch (during the end of the lock-in region) into occurring early. On the other hand, because of a small initial gap-ratio (in this case, $0.5 \lesssim g^* \lesssim 1.25$), f_{vs} modulation happens earlier and causes an early onset of the lock-in region for those cases, as shown in Fig. 15(c). However, the lock-in region is not narrowed in these cases. In this flip-flop regime of the vibrating side-by-side cylinder arrangement at Re = 100, the lock-in region ranges from $4.5 \lesssim U_r \lesssim 7.5$. With regard to an isolated vibrating cylinder at Re = 100, the lock-in region starts from $U_r \approx 5.0$ until $U_r \approx 8.0$ instead. Although f_{vs} is locked with f_n for $0.5 \lesssim g^* \lesssim 1.0$ from $4.5 \lesssim U_r \lesssim 7.5$, A_y^{max} dreadfully diminishes after $Ur \gtrsim 6$ for all vibrating side-by-side cylinder arrangements in the flip-flop regime. This is probably a result of the extremely narrow g^* when the vibration reaches its minimum position and the vortex-wake supply is suppressed by this tinny gap between cylinders. For example, A_y^{max} is about 0.42 in the present case at g^* = 0.6. The marginal distance is only 0.18, while it is 1.52 for g^* = 2.0 in the present investigation. Analogously, the vortex shedding on the inner side of a near-wall isolated oscillating cylinder is also significantly suppressed at $e^* \lesssim 0.25$ and $Re \approx 100$ in present of a strong proximity interference, where $e^* = e/D$ is the characteristic gap ratio between the flat wall and the inner side of the cylinder. Consequently,

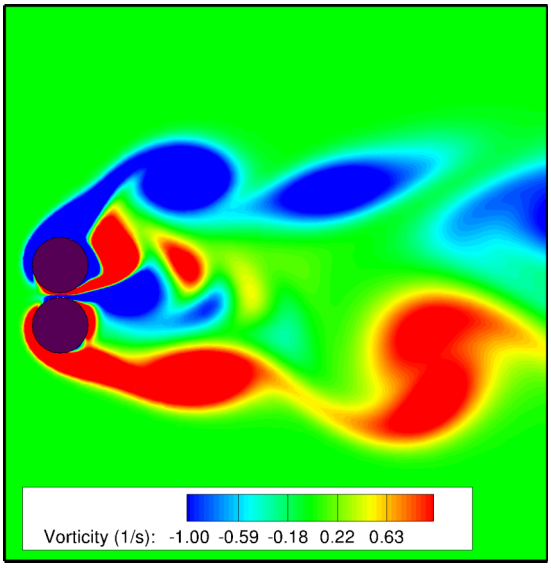

FIG. 16. Instantaneous vorticity contours in the wake of the cylinders in a side-by-side arrangement at $Re = 100$, $g^* = 0.5$, $m^* = 10$, $\zeta = 0.01$, $U_r = 5$, and $tU/D = 200$, where *Cylinder*1 vibrates in the transverse direction. The flow is from left to right.

the supply of the gap flow is cut by the tinny gap during vibration. As a result, A_y^{max} of the cases during the flip-flop regime is decreased after $U_r \gtrsim 6$. This can be visualized in Fig. 16, which is the vortex contour plot of a vibrating side-by-side cylinder arrangement of $g^* = 0.5$ at the minimum A_y ($tU/D = 200$). Furthermore, subject to the strong proximity interference, the relationship between $f^*_{A_y}$ and U_r in these g^* cases cannot agree with the Strouhal relation very well in the post-lock region.

The interaction between the gap flow and VIV is mutual and complex. The biased gap flow causes the shrinkage of the lock-in range and its early occurrence and ending through the enhanced vortex shedding frequency. On the other hand, VIV inhibits the gap flow to change its course and retains it to its side permanently. Although a vibrating cylinder is included in the side-by-side arrangement, the instantaneous g^* during vibration is still within the range of $0.3 \lesssim g^* \lesssim 1.25$. Intuitively it is peculiar why the pitchfork bifurcation is lost? However, it will be shown that one of the prerequisites of the pitchfork bifurcation does not fulfill in the vibrating side-by-side arrangement during lock-in. This will be elaborated together with the flow regime development in detail in Sec. IV D. So far although we have not revealed the root causes for the loss of the pitchfork bifurcation, it is observable that the gap flow behavior is tremendously different from that in the stationary side-by-side cylinder arrangement. Therefore, a comparison between the stationary and vibrating side-by-side arrangements is performed and plotted in Fig. 17(c). It shows the time-averaged x-component velocity profiles of the gap flow of stationary and vibrating side-by-side arrangements. It can be seen that the velocity profiles during pre- and post-lock-in are very similar and symmetric. However, the time-averaged x-component velocity mean value biases toward the vibrating cylinder during lock-in. This implies that in a time-averaged sense, the x-component of the velocity value on the upper section of the gap flow is higher than its lower section and leads the direction of the gap flow towards the vibrating cylinder. This observation is paramount to understand the deflected gap flow regime and will be discussed in Sec. IV D.

To describe the eddying motion and flow characteristic patterns, the critical-point concept (CPC) and phase-plane theory are adopted. Based on the definition from Ref. 45, critical points are points in the flow field where the streamline slope is indeterminate and the velocity is zero relative to an appropriate observer. In general, the critical points can be classified into 6 categories, namely nodal source/unstable node, nodal sink/stable node, spiral source/unstable focus, spiral sink/stable focus, (four-way indeterminant) saddle point, and (stable) center. Moreover their respective eigenvectors determine the distortion or stretching of that particular critical point and influence the shape

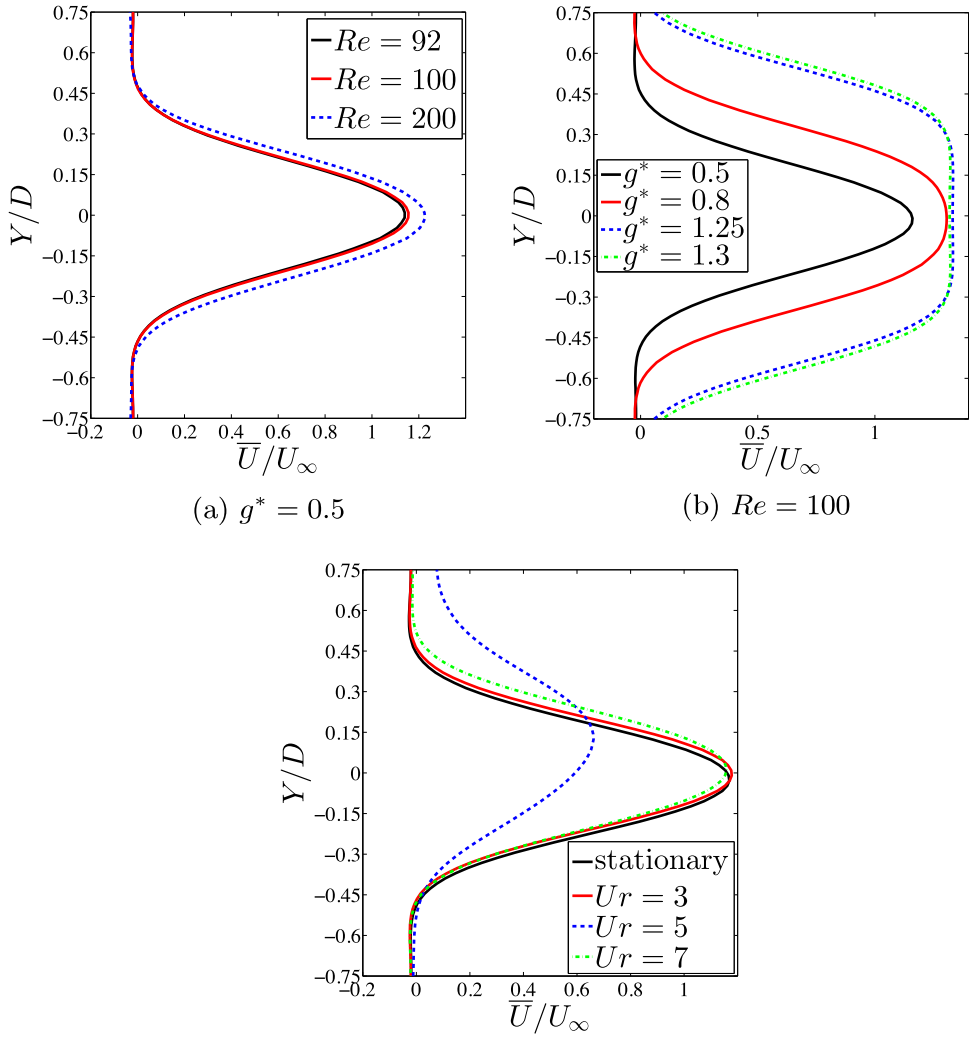

FIG. 17. Time-averaged x-component velocity profiles of gap flow in side-by-side arrangements: (a) varying Reynolds number with fixed gap ratio $g^* = 0.5$ for a stationary side-by-side arrangement, (b) different gap ratios at constant Reynolds number $Re = 100$ for stationary side-by-side, (c) vibrating side-by-side configuration for varying reduced velocity U_r. The velocity profiles are extracted in the near-wake region at locations: a vertical linear region from $(0.6D, 0.75D)$ to $(0.6D, -0.75D)$, where $(0.0D,0.0D)$ is the center between the cylinders. The time-averaging is performed from tU/D = 300 to 500.

and strength of the corresponding critical point in that particular phase planes. In a basic two dimensional steady flow problem, there are only two types of critical points exist, namely center and saddle points as labelled in Fig. 18(a). With regard to the significance of our discussion, the critical question is how the gap flow interacts with these critical points? Based on the no-cross principle of the streamline, the streamlines will always be tangent to the particular streamline with a higher magnitude of the eigenvalue. From the flow field viewpoint, this means that streamlines will cling to and follow the curvature of the streamlines of the locally fast flowing fluid regions.

With these post-processing tools, we attempt to find the coupled interactions between the gap flow and the vortex wake dynamics. It was well studied by many authors that the existence of the flip-flop in a perfect symmetric side-by-side arrangement at Reynolds number ranging from 100 to 200. However, it is also reported by Alam and Sakamoto[42] that a quasi-stable deflected gap flow regime can be achieved at this relatively higher Reynolds number range by introducing a slight

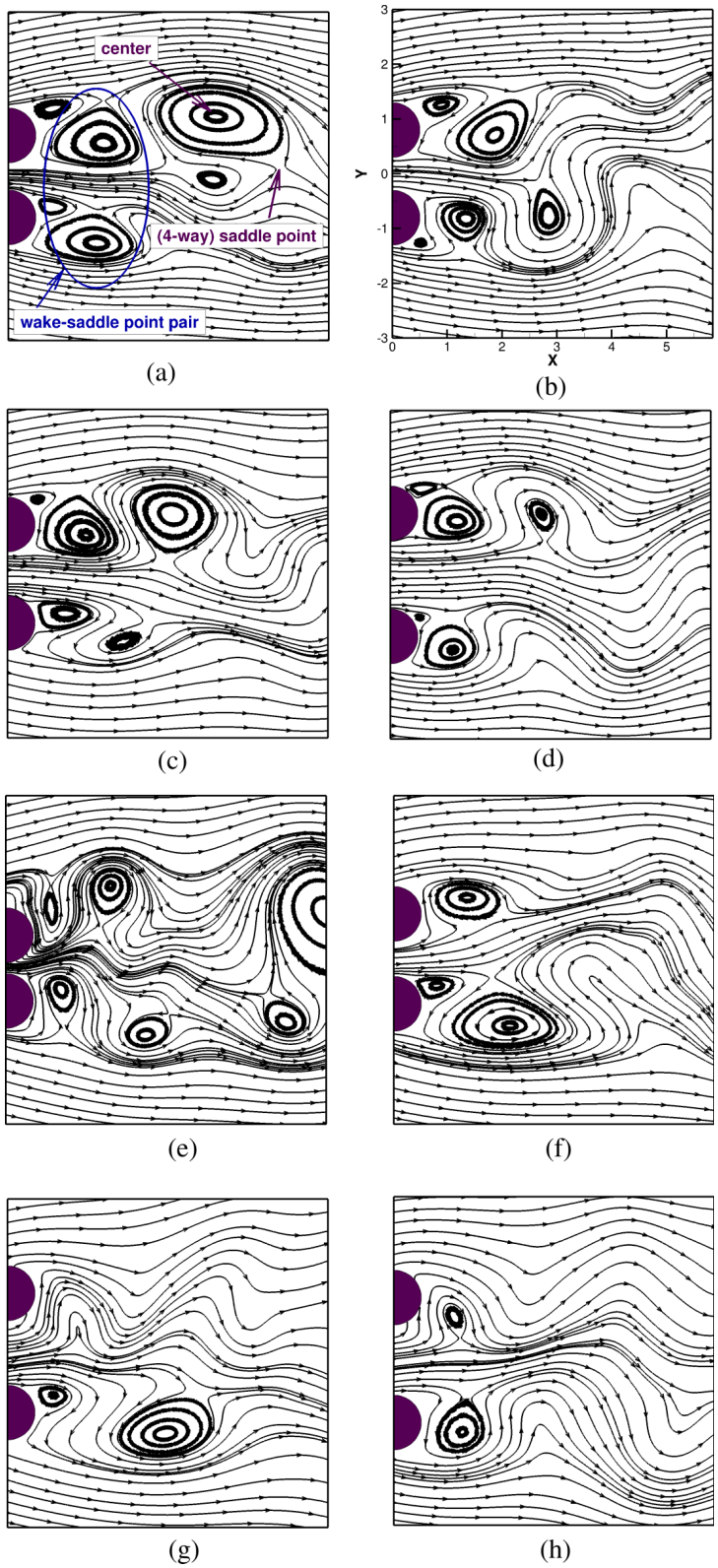

FIG. 18. Instantaneous streamline plots of the side-by-side arrangements at $Re = 100$: (a)-(d) side-by-side arrangement at $g^* \in 0.5-1.25$; (e)-(h) side-by-side arrangement at $m^* = 10$, $\zeta = 0.01$, $U_r = 5$, and $g^* \in 0.5-1.25$, where *Cylinder*1 vibrates in the transverse direction. (a) $g^* = 0.5$, (b) $g^* = 0.6$, (c) $g^* = 0.8$, (d) $g^* = 1.25$, (e) $g^* = 0.5$ and $U_r = 5$, (f) $g^* = 0.6$ and $U_r = 5$, (g) $g^* = 0.8$ and $U_r = 5$, (h) $g^* = 1.25$ and $U_r = 5$.

asymmetry into the side-by-side arrangement, e.g., angle of attack variation and different size of cylinders. In fact, the angle of attack is equivalent to a staggered arrangement with $Cylinder1$ at further downstream position. It is observed that the gap flow will be biased toward the upstream cylinder at $1.2 \lesssim t^*$ (center-to-center characteristic distance) $\lesssim 2.25$ and $100 \lesssim Re \lesssim 200$. This similarity to the stationary side-by-side arrangement is reasonable, since the deflected gap flow regime is insensitive to the bluff bodies topography. Hence, it is believed that the stable deflected gap flow regime is independent upon the angle of attack, which is beyond the scope of the present investigation. Based on the analysis of a staggered circular cylinder,[8] the outer side free shear layer of $Cylinder2$ is stretched and weakened relative to that of $Cylinder1$. Analytically, this stretching from a particular eigenvector of a center (vortex wake) means that the strength of this wake is relatively weak in this phase-plane. This observation may imply that the deflection of the gap flow is related to the strength of the pair of vortex wakes from cylinders. On the other hand, through the observation in the staggered cylinders in which a flip-flop exists, four-way saddle points can also be observed periodically in the normal path of the gap flow in the near-wake region. Hence, it is understandable that the gap flow will deflect toward the opposite direction of the saddle point.

Inspired by these observations, a similar investigation is performed on stationary side-by-side arrangements, as shown in Fig. 18 from (a) to (d). One can observe that every deflecting corner of the gap flow is associated with a four-way saddle point of a local strong vortex wake. Therefore, the velocity magnitude at these four-way saddle point should be a local minimum, as plotted in Fig. 19. It shows that the saddle points and center locate exactly at the low velocity magnitude regions. Based on the no-cross principle, the gap flow streamlines deflect along the streamlines radiating from the saddle point and its direction is led by the relatively fast flowing shear layers. Similar to a pair of staggered cylinders, these four-way saddle points also intermittently appear on the straight path of the gap flow in the near-wake region. The streamlines which form the gap flow adapt themselves along the curvature of the relative strong local vortex wake, since the velocity on the outer layer of these wakes is relatively higher. If the saddle point is formed by one particular strong wake on one side (it is the side of the wider near-wake region), the gap flow is deflected to the opposite direction. Qualitatively, the near-wake region manifests a deflected gap flow regime.

Since the anti-phase vortex shedding is dominant, *vortex-wake pairs*, as shown in Fig. 18(b), can be observed much frequently in the near-wake region. In the unbalance of the near-wake region, the strength of the vortex wake pairs is different on both sides. The gap flow will adapt to the curvature of the stronger local vortex wake, since there is a larger gradient across its outer shear layers. The strong wakes in the near-wake region is associated with the wider near-wake region. However, this is not the case during the switch-over of the gap flow. At the instant of the flip-flop, the in-phase vortex synchronization is dominant. Instead of *vortex-wake pairs* in the near-wake region, *vortex wake-saddle point pairs* appear, as shown in Fig. 18(a). Following the curvature of the vortex wake and the opposite direction of the saddle point, the gap flow sweeps up and down. As the re-occurrence of wide and narrow near-wake regions, the gap flow is eventually stabilized to one side and forms a stable deflected gap flow regime again. In a nutshell, the path of the gap flow is dependent upon the dynamics of saddle points and the relative strength of the vortex wakes.

The quasi-stable deflected gap flow regime in a vibrating side-by-side cylinder can be understood in a similar approach. It has been mentioned earlier that the gap flow deflects toward the vibrating cylinder in a quasi-stable manner during lock-in, as shown in Fig. 18 from (e) to (h). As $Cylinder1$ vibrates extensively, the vortex wakes formed from the outer side of the $Cylinder1$ are stretched/weakened and brought farther away from the straight path of the gap flow. Therefore, the gap flow is pushed relatively upper toward the vibrating cylinder ($Cylinder1$) by this relatively strong local wake from the inner side of $Cylinder2$. It is well known that the stable deflected gap flow regime possesses two different frequencies on each cylinder of the side-by-side arrangement. Nonetheless, the frequencies on both cylinders are synchronized to an identical value in vibrating side-by-side cylinders during frequency lock-in and a large single vortex street is formed farther downstream through an in-phase vortex synchronization. As a result of this frequency synchronization and the observed anti-phase vortex synchronization in the near-wake region, *vortex-wake pairs*,

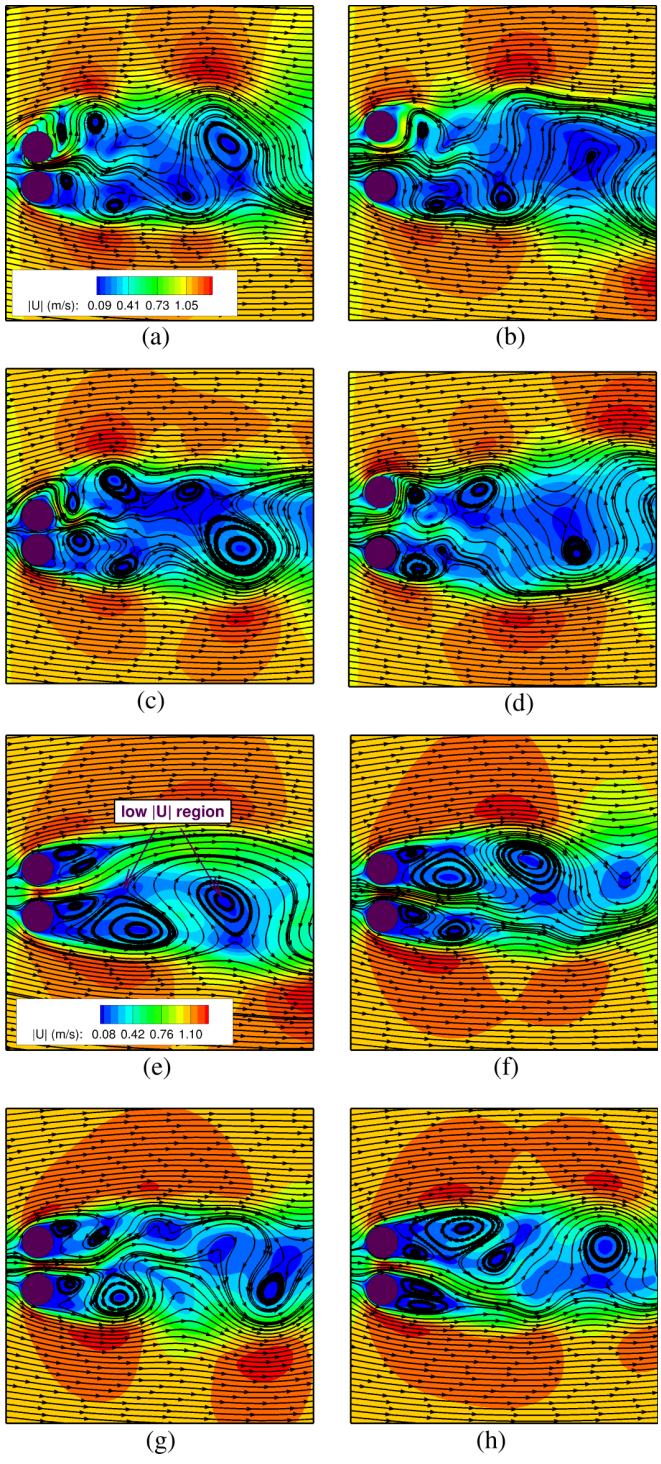

FIG. 19. Streamline and velocity magnitude contour plots of the side-by-side arrangements at $Re = 100$ and $g^* = 0.5$: (a)-(d) side-by-side arrangements; (e)-(h) vibrating side-by-side arrangements at $m^* = 10$, $\zeta = 0.01$, and $U_r = 5$, where *Cylinder*1 vibrates in the transverse direction.

the anti-phase vortex shedding is retained. There is no chance for the flip-flop to develop. These findings are further validated through the modal analysis of the vibrating side-by-side arrangement. As discussed in Sec. IV C, the low frequency DMD modes which are associated with the deflected gap flow regime and flip-flop cannot be extracted as influential DMD modes.

D. Further discussion on the dependency and origin of the flip-flop

The gap flow is significantly suppressed at $g^* \lesssim 0.3$ and there is only one large von Kármán vortex street forming farther downstream of the pair of side-by-side cylinders. Therefore, the entire arrangement can be considered as a single bluff body with base-bleeding flow. The complexity in the flow regime raises as the gap ratio increases. The flip-flop and deflected gap flow regime are introduced as additional interferences to the coupled near-wake region at $g^* \in 0.3 - 1.25$. As discussed in Sec. IV A, the flip-flop is a secondary instability from the coupling between pitch-fork bifurcation and Hopf bifurcation. The development and position of the Hopf bifurcation are significantly dependent upon the Reynolds number. As a result, the flip-flop occurs beyond a critical Reynolds number, $Re \gtrsim 92$, in a stationary side-by-side cylinder arrangement at $g^* = 0.5$. The next question could be whether the flip-flop is really a chaos without a regular pattern when exceeding critical parameters? If it is not, what do its behaviors depend upon at various side-by-side arrangements?

To answer these questions, we recollect all the results obtained in the present investigation to shed light on the flip-flop behavior of the gap flow. Comparing Figs. 17(b) and 20, it is observed that as g^* increases in the flip-flop regime, the strength of the x-component velocity, $|U|$, of the gap flow and f_{flip} increase spontaneously. Therefore, we believe that f_{flip} has a dependency on the gap

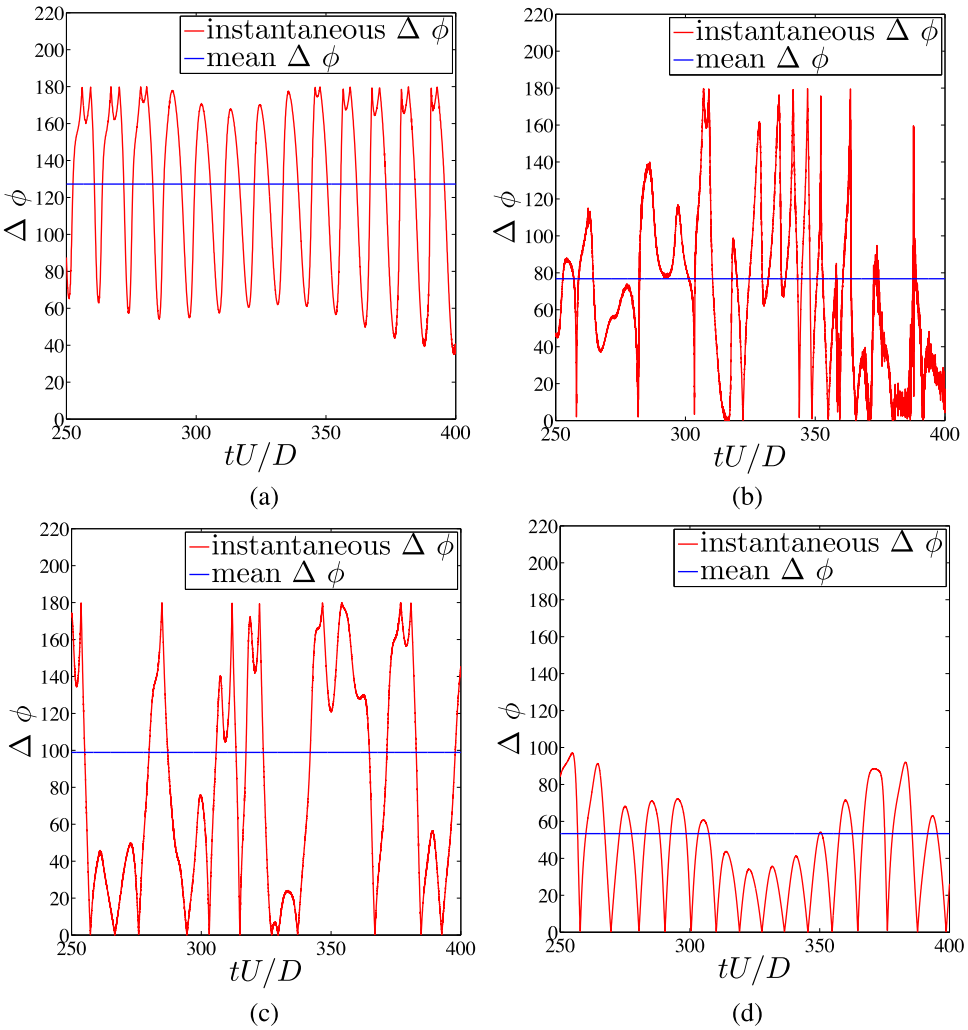

FIG. 20. Time history of the instantaneous phase angle difference of C_l of stationary cylinders in a side-by-side arrangement at $Re = 100$ and $g^* \in 0.3 - 1.25$. (a) $g^* = 0.3$, (b) $g^* = 0.5$, (c) $g^* = 0.8$, (d) $g^* = 1.25$.

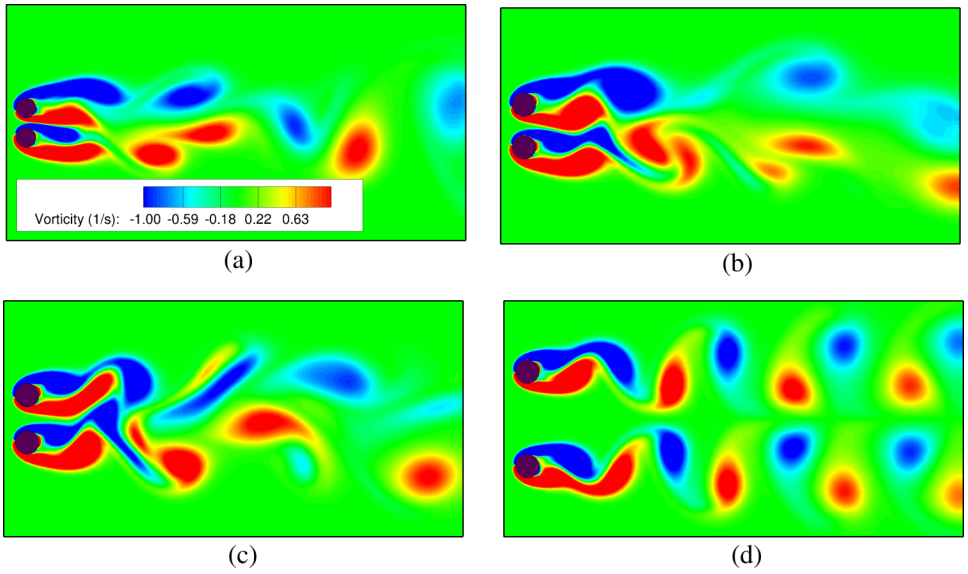

FIG. 21. Vorticity contour plots of stationary cylinders in a side-by-side arrangement at $Re = 100$: g^* = (a) 0.5, (b) 0.8, (c) 1.0, (d) 3.0.

flow strength which rises as g^* increases in the flip-flop regime. In Fig. 21 from (a) to (c), through qualitative observation, the merging distance of vortex wakes (x^*_{cr}=x_{cr}/D), the length measured from the point ($0.0D$,$0.0D$) until the downstream distance where the in-phase vortex synchronization starts forming, possesses a gradually incremental tendency as g^* increases. On the other hand, x^*_{cr} is not observable in the measurable distance outside the flip-flop regime at $g^* \gtrsim 1.25$ as shown in Fig. 21(d). It implies that x^*_{cr} is dynamic and also depends on the gap flow strength. Furthermore, x^*_{cr} is paramount in flip-flop dynamics since it represents one of the critical parameters for the formation of the in-phase synchronization in a side-by-side arrangement. Therefore, the focus is to explore the relationship between the flip-flop, the gap ratio g^*, and the vortex merging distance x^*_{cr}.

It is known that the flip-flop is completely suppressed at $g^* \lesssim 0.3$ and disappears after $g^* \gtrsim 1.25$. Fig. 20 clearly shows the flip-flopping moments in the stationary side-by-side cylinders at $Re = 100$. The flip-flop frequency f_{flip} is indeed much lower at smaller g^*, where the gap flow strength is feeble and possibly suppressed at $g^* = 0.3$. Furthermore, the strength of the gap flow is also enhanced in the proportion of Reynolds number, as shown in Fig. 17(a). Observing from its corresponding time history plot of flip-flopping moment through HHT in Fig. 22, the flip-flop frequency f_{flip} is increased at a higher Re value in the two-dimensional laminar flow. Therefore, it is believed that f_{flip} is gap flow strength dependent, which is associated with both the Reynolds number Re and gap ratio g^*.

It is intuitive that each cylinder in a side-by-side arrangement behaves more like an isolated vibrating cylinder at large gap ratio $g^* \gtrsim 3$ or 4. The single von Kármán vortex street disappears. Instead, two vortex streets form behind each cylinder and the flip-flop fades away. However, the kinematics of the flip-flop requires more detailed investigation of the gap ratio g^*, the vortex merging distance x^*_{cr}, and the phase difference ϕ. As mentioned earlier in this section, it is qualitatively observed in Fig. 21 that x^*_{cr} gradually increases as the increment of g^*. This is confirmed quantitatively through the exact measurement of x^*_{cr} in a time-averaged manner at different g^* in Fig. 23(a). In fact, x^*_{cr} dynamically changes in different circumstances. As shown in Fig. 23(a), x^*_{cr} of the in-phase vortex shedding refers to the critical distance during flip-flop. Meanwhile, its counterpart for a perfect anti-phase vortex shedding pair also grows proportionally with g^* and manifest at farther downstream. Different from x^*_{cr} for the location of the Hopf bifurcation, it refers to the earliest vortex merging distance in a perfect anti-phase vortex wake pair. It implies that the position of the Hopf bifurcation should be even farther away from this nondimensional distance during the anti-phase vortex shedding. It is already elaborated that the flip-flop is a result of coupling

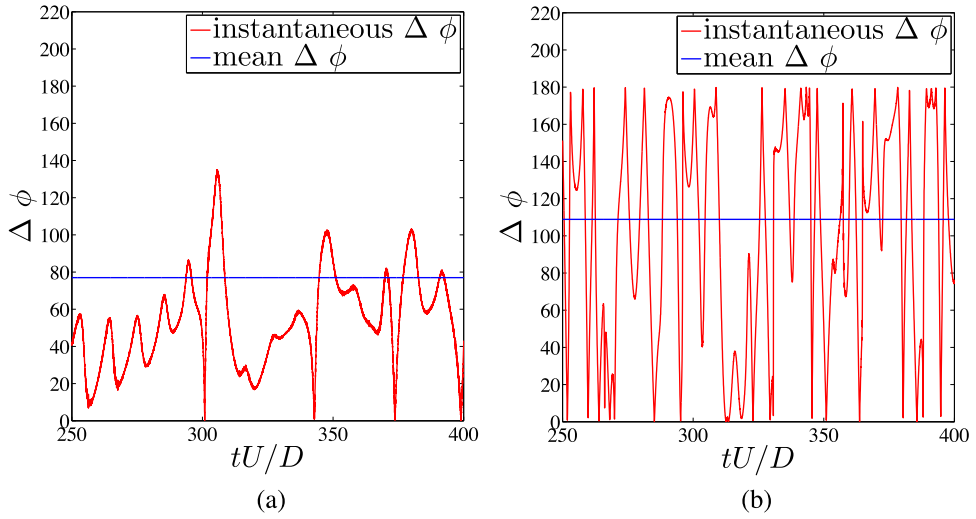

FIG. 22. Time history of the instantaneous phase angle difference of C_l of stationary cylinders in a side-by-side arrangement at $g^* = 0.5$: Re = (a) 92, (b) 200.

between the pitchfork and Hopf bifurcations. A larger distance between them during anti-phase vortex shedding indicates that the possibility of flip-flop is low. For the ease of measurement, two approximating polynomial equations of the x^*_{cr} evolution, Eqs. (34) and (35) for the anti-phase and in-phase vortex shedding, respectively, are given as follows:

$$x^*_{cr} = -0.9649g^{*4} + 6.2138g^{*3} - 13.957g^{*2} + 16.84g^* - 1.1421, \tag{34}$$

$$x^*_{cr} = 0.2134g^{*4} - 1.1097g^{*3} + 2.8631g^{*2} - 0.9426g^* + 3.3848. \tag{35}$$

In fact, a perfect anti-phase vortex shedding pattern is barely observed in the flip-flop regime of side-by-side arrangements. The phase $\Delta\phi$ of C_l dynamically switches between the in-phase and anti-phase as time evolves. As a result, the distance x^*_{cr} changes correspondingly as well. To investigate the disappearance of the flip-flop during lock-in in the vibrating side-by-side arrangement, the time-averaged x^*_{cr} at three typical instants, the flip-flop, the deflected gap flow regime and the lock-in, is plotted in Fig. 23(b). The merging distance x^*_{cr} during the flip-flop is identical to

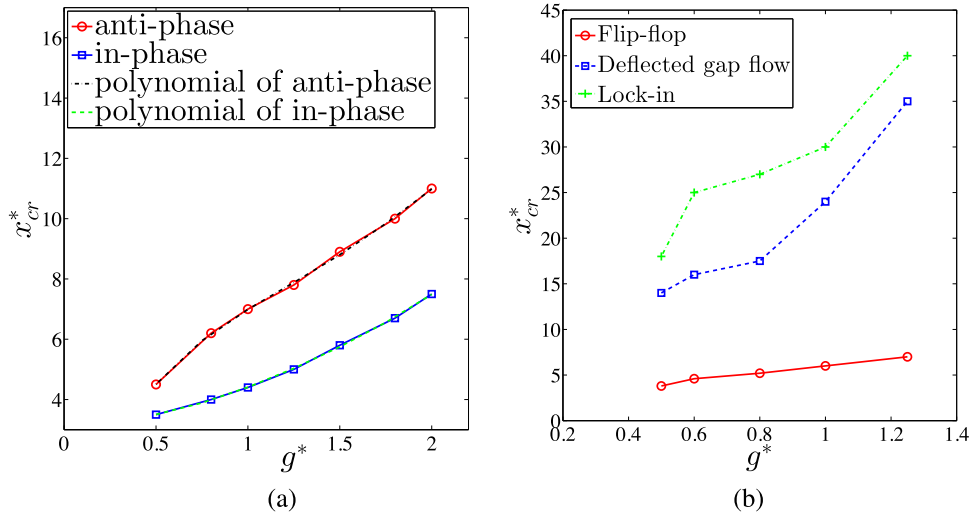

FIG. 23. Relationship between the vortex merging distance x^*_{cr} and gap ratio g^*: (a) side-by-side arrangements at Re = 100 and $g^* \in 0.5-2.0$; (b) side-by-side arrangements at $m^* = 10$, $\zeta = 0.01$, and $g^* \in 0.5-1.25$, where *Cylinder*1 vibrates in the transverse direction.

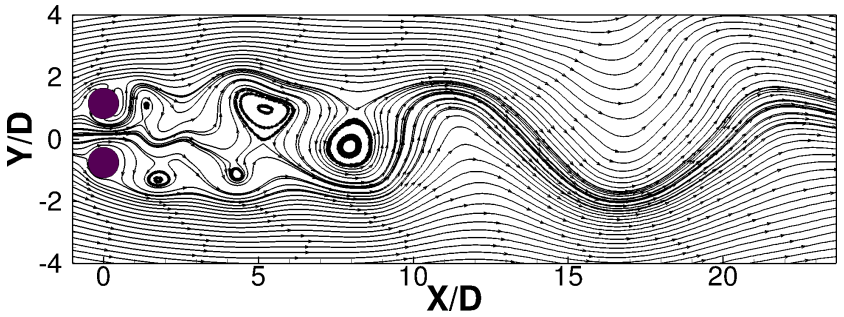

FIG. 24. Streamline plot of cylinders in a side-by-side arrangement at $Re = 100$, $m^* = 10$, $\zeta = 0.01$, $g^* = 0.5$, and $U_r = 5$, where *Cylinder*1 vibrates in the transverse direction.

its stationary counterpart during in-phase vortex synchronization, as plotted in Fig. 23(a). On the other hand, x^*_{cr} in the deflected gap flow regime is much larger. This is illustrated via DMD modal analysis, streamline plot, and x^*_{cr} analysis. For instance, the in-phase vortex synchronization for $Re = 100$, $g^* = 0.5$, and $U_r = 5$ upsurges after $15D$ downstream in Figs. 12(a) and 12(c). It can also be observed through its streamline plot in Fig. 24 that a large regular von Kármán vortex street forms after $15D$ downstream. It is noticed that these time-averaged x^*_{cr} values are not noticeably influenced at U_r from 0 to 10 in the current work. Its counterpart at the stationary side-by-side arrangement also shows $x^*_{cr} \approx 18$ in Fig. 23(b). Therefore, it is believed that the plotted x^*_{cr} is valid to indicate the position of the Hopf bifurcation in side-by-side arrangements. Since there is a significant segregation of the pitchfork bifurcation and Hopf bifurcation, the flip-flop should be significantly suppressed after the flow field transition into the deflected gap flow regime. However, the vortex shedding frequency f_{vs} on each cylinder is dynamically modulated by the dynamics of the gap flow. As a result, $\Delta\phi$ is constantly changing between 0° and 180° as shown in Figs. 7(d), 20(b)–20(d), and 22(b). When $\Delta\phi$ approaches zero, the Hopf bifurcation manifest itself again in the near-wake region at a very close x^*_{cr} and the flip-flop is triggered.

Based on the discussion in the previous paragraph, we have a quantitative understanding on the origin of the disappearance of the flip-flop during the lock-in of vibrating side-by-side arrangements. Fig. 23(b) shows an even farther downstream vortex merging distance during lock-in. It is believed that the likelihood of the flip-flop is even more sparse. Furthermore, since the vortex shedding frequency f_{vs} on each cylinder is synchronized to f_n, the phase $\Delta\phi$=0 is unlikely to be without frequency modulation and $\Delta\phi$ will retain at about 90°, as shown in Fig. 11(d). Therefore, the flip-flop is not observed during the lock-in of vibrating side-by-side arrangements. However although the gap flow deflects, f_{vs} on each cylinder is identical. This is different from the characteristics in the aforementioned deflected gap flow regime, in which narrow and wide near-wake regions are formed and the frequency enhancement is observed in the narrow one. To shed some light, the time-averaged x-component velocity profiles of the gap flow at $Re = 100$ and $g^* = 0.5$ at different U_r are plotted in Fig. 17(c). It shows that the velocity profiles are symmetry in the present of benign motion during pre- and post-lock-in, except the one during frequency lock-in. This asymmetry of flow field is not observed in the previously reported deflected gap flow regime. Therefore, the deflected gap flow regime probably breaks down by the asymmetry of gap flow during the frequency lock-in. It means that not only the Hopf bifurcation is developed farther downstream, but the pitchfork bifurcation breaks down during the frequency lock-in of vibrating side-by-side arrangements as well.

V. CONCLUDING REMARKS

The present study investigated the interaction between the gap flow and VIV in a pair of side-by-side circular cylinders, whereby one cylinder was stationary and its counterpart was free to vibrate in the transverse direction. The gap flow dynamics in the stationary side-by-side circular cylinder arrangements was first reviewed and investigated using the wake flow visualization

together with the spectral (HHT) and modal (SP-DMD) analysis techniques. Three flow regimes namely, single-bluff-body regime ($g^* \lesssim 0.3$), biased-flow/flip-flop regime ($0.3 \lesssim g^* \lesssim 1.25$), and parallel-vortex-street regime ($1.25 \lesssim g^* \lesssim 1.5$) are shown with regard to the gap flow dynamics at $Re = 100$. The focus has been placed on the flip-flop regime, in which there is a strong gap flow formation with a low pressure region in the kernel of the gap flow. In the flip-flop regime, the gap flow deflected toward one side of cylinders and switched over its direction intermittently. In the deflected gap flow regime, a narrower near-wake region associated with a higher f_{vs} and C_d due to the enhanced vortex interaction and vice versa. A complex beating phenomenon was observed in this regime. It was believed to be originated from this two-frequency flow regime caused by the gap flow instability. As reported, the pitchfork and Hopf bifurcations were associated with the deflected gap flow behavior and in-phase synchronization, respectively. In particular, the flip-flop secondary instability, originated by the coupling of pitchfork and Hopf bifurcations as spontaneous symmetry breaking, was visualized through the modal analysis based on SP-DMD for a range of Reynolds numbers. We found that the flip-flop occurs at gap ratio $g^* = 0.5$ after $Re \approx 92$, when the pitchfork and Hopf bifurcation regions superimpose. The exact moment of the flip-flop was also quantified through the HHT analysis. The representative characteristic DMD modes of the pitchfork bifurcation, Hopf bifurcation, and the flip-flop are extracted using SP-DMD for significant influential modes.

Following the investigation for the stationary side-by-side arrangement, the gap flow and VIV interaction in the vibrating side-by-side arrangements was investigated in a similar fashion. It was found that the gap flow quasi-stably deflected toward the vibrating cylinder during the VIV frequency lock-in. This was confirmed by analyzing the phase information $\Delta\phi(t)$ of C_l using the HHT analysis, in which the flip-flop ($\Delta\phi = 0$) never occurred. Instead of the pitchfork bifurcation, it is believed to be caused by an unbalanced gap flow strength in the near-wake region. On the other hand, in the pre- and post-lock-in regions, the flip-flop is still conspicuous similar to the stationary side-by-side arrangements, although the vibrations of the cylinder were still significant. The gap flow interference on VIV dynamics was found to be significant. There were premature onset and ending of the lock-in region owing to the gap flow interference in the flip-flop regime. The lock-in region could be reduced by 43% approximately in some cases. This was confirmed through the analysis between the frequency ratio $f^*_{A_y}$ and the reduced velocity U_r. On the contrary, in the pre- and post-lock-in regimes, the mutual VIV and gap flow interference is not very significant compared with the results of their corresponding stationary side-by-side counterparts. The gap flow x-component velocity profiles during pre- and post-lock-in are very symmetric and resembling that of the corresponding stationary setup. However, since the transverse amplitude A_y is still significant during post-lock-in, their frequency responses did not follow the Strouhal relation.

The flip-flop was found to be a function of the gap flow strength, whereby the flip-flop frequency f_{flip} gradually increased as a function of the gap ratio g^* and Reynolds number Re. The symmetry of the gap flow strength and the coupling of the pitchfork and Hopf bifurcations are the two prerequisites to the flip-flopping phenomenon. Through DMD analysis, it was shown that the DMD modes of the in-phase vortex synchronization was pushed further downstream and detached with the pitchfork bifurcation region. This was confirmed through the DMD modal analysis, the vortex merging distance x^*_{cr} analysis, and the streamline plots. Two representative correlation expressions were also introduced for the critical vortex merging distance. Therefore, as the detachment of two bifurcations and the breakdown of the pitchfork bifurcation, the flip-flop disappeared during the lock-in of the vibrating side-by-side arrangements. The origins of the deflected gap flow regime and the flip-flopping phenomenon were further studied using the critical-point concept. With the absence of source terms in the classical two dimensional cross flow problems, a strong vortex wake is normally associated with a stable center and four-way indeterminant saddle point. Because of the large velocity gradient on the outer ring of the strong wake and indeterminacy of its saddle point, the fluid gap was guided or deflected to a particular direction. There were saddle points observed intermittently in the middle path of the stationary side-by-side arrangements within the flip-flop regime. Therefore, the path of the gap flow is indeterminant and switch its course intermittently. On the other hand, the saddle point is always absent during the lock-in of the vibrating

side-by-side arrangement and the gap flow was guided to the side of the vibrating cylinder permanently. As a result, the flip-flop was not observed. In future, interactions between the flip-flop and vortex-induced vibration will be investigated in detail at higher Reynolds number.

ACKNOWLEDGMENTS

The first author would like to thank Singapore Maritime Institute Grant No. (SMI-2014-OF-04) for the financial support.

[1] P. W. Bearman and A. J. Wadcock, "The interaction between a pair of circular cylinders normal to a stream," J. Fluid Mech. **61**(03), 499–511 (1973).
[2] M. M. Zdravkovich, "The effects of interference between circular cylinders in cross flow," J. Fluids Struct. **1**(2), 239–261 (1987).
[3] J. C. Lin, Y. Yang, and D. Rockwell, "Flow past two cylinders in tandem: Instantaneous and averaged flow structure," J. Fluids Struct. **16**(8), 1059–1071 (2002).
[4] M. Springer, R. K. Jaiman, S. Cosgrove, and Y. Constantinides, "Numerical modeling of vortex-induced vibrations of two flexible risers," ASME Offshore Mechanics and Arctic Engineering OMAE09-79801 CP, 2009.
[5] R. C. Mysa, A. Kaboudian, and R. K. Jaiman, "On the origin of wake-induced vibration in two tandem circular cylinders at low Reynolds number," J. Fluids Struct. **61**, 76–98 (2016).
[6] D. Sumner, S. S. T. Wong, S. J. Price, and M. P. Paidoussis, "Fluid behaviour of side-by-side circular cylinders in steady cross-flow," J. Fluids Struct. **13**(3), 309–338 (1999).
[7] S. Kang, "Characteristics of flow over two circular cylinders in a side-by-side arrangement at low Reynolds numbers," Phys. Fluids **15**(9), 2486–2498 (2003).
[8] D. Sumner, S. J. Price, and M. P. Paidoussis, "Flow-pattern identification for two staggered circular cylinders in cross-flow," J. Fluid Mech. **411**, 263–303 (2000).
[9] M. P. Paidoussis, "Fluidelastic vibration of cylinder arrays in axial and cross flow: State of the art," J. Sound Vib. **76**(3), 329–360 (1981).
[10] D. S. Weaver and J. A. Fitzpatrick, "A review of cross-flow induced vibrations in heat exchanger tube arrays," J. Fluids Struct. **2**(1), 73–93 (1988).
[11] O. M. Griffin and S. E. Ramberg, "Some recent studies of vortex shedding with application to marine tubulars and risers," J. Energy Resour. Technol. **104**(1), 2–13 (1982).
[12] A. Khalak and C. H. K. Williamson, "Motions, forces and mode transitions in vortex-induced vibrations at low mass-damping," J. Fluids Struct. **13**(7), 813–851 (1999).
[13] H. M. Blackburn, R. N. Govardhan, and C. H. K. Williamson, "A complementary numerical and physical investigation of vortex-induced vibration," J. Fluids Struct. **15**(3), 481–488 (2001).
[14] T. Sarpkaya, "A critical review of the intrinsic nature of vortex-induced vibrations," J. Fluids Struct. **19**(4), 389–447 (2004).
[15] C. H. K. Williamson and R. Govardhan, "Vortex-induced vibrations," Annu. Rev. Fluid Mech. **36**, 413–455 (2004).
[16] R. D. Gabbai and H. Benaroya, "An overview of modeling and experiments of vortex-induced vibration of circular cylinders," J. Sound Vib. **282**(3), 575–616 (2005).
[17] D. Sumner, "Two circular cylinders in cross-flow: A review," J. Fluids Struct. **26**(6), 849–899 (2010).
[18] P. W. Bearman, "Circular cylinder wakes and vortex-induced vibrations," J. Fluids Struct. **27**, 648–658 (2011).
[19] M. Braza, P. Chassaing, and H. H. Minh, "Numerical study and physical analysis of the pressure and velocity fields in the near wake of a circular cylinder," J. Fluid Mech. **165**, 79–130 (1986).
[20] S. Mittal, V. Kumar, and A. Raghuvanshi, "Unsteady incompressible flows past two cylinders in tandem and staggered arrangements," Int. J. Numer. Methods Fluids **25**(11), 1315–1344 (1997).
[21] M. Coutanceau and J. R. Defaye, "Circular cylinder wake configurations: A flow visualization survey," Appl. Mech. Rev. **44**(6), 255–305 (1991).
[22] R. K. Jaiman, F. Shakib, O. Oakley, and Y. Constantinides, "Fully coupled fluid-structure interaction for offshore applications," in *ASME 2009 28th International Conference on Ocean, Offshore and Arctic Engineering* (American Society of Mechanical Engineers, 2009), pp. 757–765.
[23] S. Ishigai, E. Nishikawa, K. Nishimura, and K. Cho, "Experimental study on structure of gas flow in tube banks with tube axes normal to flow: Part 1, kármán vortex flow from two tubes at various spacings," Bull. JSME **15**(86), 949–956 (1972).
[24] C. H. K. Williamson, "Evolution of a single wake behind a pair of bluff bodies," J. Fluid Mech. **159**, 1–18 (1985).
[25] H. J. Kim, "Investigation of the flow between a pair of circular cylinders in the flopping regime," J. Fluid Mech. **196**, 431–448 (1988).
[26] V. Joshi, B. Liu, and R. K. Jaiman, "Flow-induced vibrations of riser array system," Proceedings of the ASME 2016 35th International Conference on Ocean, Offshore and Arctic Engineering OMAE 2016.
[27] Md. Mahbub Alam and Y. Zhou, "Intrinsic features of flow around two side-by-side square cylinders," Phys. Fluids **25**(8), 085106 (2013).
[28] D. M. Y. Tham, P. S. Gurugubelli, Z. Li, and R. K. Jaiman, "Freely vibrating circular cylinder in the vicinity of a stationary wall," J. Fluids Struct. **59**, 103–128 (2015).
[29] N. E. Huang, Z. Shen, S. R. Long, M. C. Wu, H. H. Shih, Q. Zheng, N.-C. Yen, C. C. Tung, and H. H. Liu, "The empirical mode decomposition and the hilbert spectrum for nonlinear and non-stationary time series analysis," Proc. R. Soc. London, Ser. A **454**, 903–995 (1998).
[30] M. R. Jovanovic, P. J. Schmid, and J. W. Nichols, "Sparsity-promoting dynamic mode decomposition," Phys. Fluids **26**(2), 024103 (2014).

[31] R. K. Jaiman, S. Sen, and P. S. Gurugubelli, "A fully implicit combined field scheme for freely vibrating square cylinders with sharp and rounded corners," Comput. Fluids **112**, 1–18 (2015).
[32] R. K. Jaiman, N. R. Pillalamarri, and M. Z. Guan, "A stable second-order partitioned iterative scheme for freely vibrating low-mass bluff bodies in a uniform flow," Comput. Methods Appl. Mech. Eng. **301**, 187–215 (2016).
[33] R. K. Jaiman, M. Z. Guan, and T. P. Miyanawala, "Partitioned iterative and dynamic subgrid-scale methods for freely vibrating square-section structures at subcritical Reynolds number," Comput. Fluids **133**, 68–89 (2016).
[34] Y. Saad and M. H. Schultz, "GMRES: A generalized minimal residual algorithm for solving nonsymmetric linear systems," SIAM J. Sci. Stat. Comput. **7**(3), 856–869 (1986).
[35] P. J. Schmid, "Dynamic mode decomposition of numerical and experimental data," J. Fluid Mech. **656**, 5–28 (2010).
[36] M. Carini, F. Giannetti, and F. Auteri, "On the origin of the flip–flop instability of two side-by-side cylinder wakes," J. Fluid Mech. **742**, 552–576 3 (2014).
[37] I. Borazjani and F. Sotiropoulos, "Vortex-induced vibrations of two cylinders in tandem arrangement in the proximity–wake interference region," J. Fluid Mech. **621**, 321–364 (2009).
[38] Y. Bao, C. Huang, D. Zhou, J. Tu, and Z. Han, "Two-degree-of-freedom flow-induced vibrations on isolated and tandem cylinders with varying natural frequency ratios," J. Fluids Struct. **35**, 50–75 (2012).
[39] T. K. Prasanth, S. Behara, S. P. Singh, R. Kumar, and S. Mittal, "Effect of blockage on vortex-induced vibrations at low Reynolds numbers," J. Fluids Struct. **22**(6), 865–876 (2006).
[40] Z. Li, W. Yao, K. Yang, R. K. Jaiman, and B. C. Khoo, "On the vortex-induced oscillations of a freely vibrating cylinder in the vicinity of a stationary plane wall," J. Fluids Struct. **65**, 495–526 (2016).
[41] H. Baek and G. E. Karniadakis, "Suppressing vortex-induced vibrations via passive means," J. Fluids Struct. **25**(5), 848–866 (2009).
[42] M. M. Alam and H. Sakamoto, "Investigation of strouhal frequencies of two staggered bluff bodies and detection of multi-stable flow by wavelets," J. Fluids Struct. **20**(3), 425–449 (2005).
[43] J. Mizushima and Y. Ino, "Stability of flows past a pair of circular cylinders in a side-by-side arrangement," J. Fluid Mech. **595**, 491–507 (2008).
[44] I. Peschard and P. Le Gal, "Coupled wakes of cylinders," Phys. Rev. Lett. **77**(15), 3122 (1996).
[45] A. E. Perry and M. S. Chong, "A description of eddying motions and flow patterns using critical-point concepts," Annu. Rev. Fluid Mech. **19**(1), 125–155 (1987).